Quaternary Science Reviews 269 (2021) 107134

Contents lists available at ScienceDirect

Quaternary Science Reviews

journal homepage: www.elsevier.com/locate/quascirev

Last millennium climate variability of the varved Lake Jeinimeni geochemical record from NE Chilean Patagonia

N. Fagel [a, *], P. Pedreros [b], D. Alvarez [b, c], W. Tylmann [d], O. Namur [e], A.C. Da Silva [f], P. Jana [b], A. Araneda [b], I. Billy [g], S. Schmidt [g], R. Urrutia [b]

[a] Université de Liège, AGEs, Argiles, Géochimie et Environnements Sédimentaires, Department of Geology, 4000, Liège, Belgium
[b] University of Concepcion, Faculty of Environmental Sciences and EULA, Chile Environmental Sciences Centre, Concepcion, Chile
[c] Universidad Santo Tomás, Facultad de Ciencias, Concepcion, Chile
[d] University of Gdansk, Faculty of Oceanography and Geography, Poland
[e] KU Leuven University, Department of Earth and Planetary Sciences, 3001, Heverlee, Belgium
[f] Université de Liège, Sedimentary Petrology, Department of Geology, 4000, Liège, Belgium
[g] Université de Bordeaux, UMR Environnements et Paléoenvironnements Océaniques et Continentaux, France

ARTICLE INFO

Article history:
Received 26 March 2020
Received in revised form
8 March 2021
Accepted 1 August 2021
Available online 21 August 2021

Handling Editor: I. Hendy

Keywords:
Lacustrine sediment
Clastic varves
Climate variability
XRF-Core scanner
Late Holocene

ABSTRACT

Paleoclimate studies in Patagonia show a high Holocene climate variability, strongly controlled by the intensity and latitudinal position of the Southern Westerly Winds. In this study, environmental and climate variability, and in particular winter precipitation, was reconstructed over the last centuries through sedimentological and geochemical analyses of a core from Lake Jeinimeni in North East Patagonia. Visual description, X-ray radiographies and thin section observations point to finely laminated sediments, made by fine sands and light brown clayey silts forming an annual deposition (varves) occasionally interrupted by two Hudson volcano-related tephras and 15 pluri-millimetre to pluri-centimetre coarser sandy to gravely layers. Varve counting confirmed by ^{210}Pb and ^{137}Cs indicates a detrital sequence of at least 750 yr. Based on a correlation with local meteorological data for the 1930–1988AD interval, varve thickness and statistical treatment of XRF geochemical data give information on transport pathway and sedimentary deposit conditions. The sandy laminae correspond to the deposition of high sedimentary load delivered by austral spring snowmelt whereas the clayey silt laminae result of particle settling in the water column during low hydrodynamical conditions. Thicker varves observed in dry conditions underline the importance of aeolian transport in sedimentary deposition. During locally dry and windy summer, the wind may erode and remobilise the sedimentary deposits along the lake margins. The sandy and gravely layers record massive erosional events due to proximal watershed perturbation driven by climatic or tectonic mechanisms. The clastic varves of Lake Jeinimeni document environmental decadal to multidecadal variability in East Patagonia over the last centuries. The more pronounced sediment transition around 1750 CE is consistent with the inception of the Little Ice Age-type event, in agreement with North Patagonian paleoclimate reconstructions derived from glacier advances, lacustrine varve thickness and tree-ring records.

1. Introduction

Holocene climate variability at the southernmost tip of South America is strongly controlled by the latitudinal position and intensity of the Southern Westerlies Winds (SWW; Markgraf, 1993; Gilli et al., 2005; Garreaud et al., 2009; among others). SWW are associated to storm tracks bringing heavy rainfalls (Trenbeth, 1991). At present, these winds bring precipitation over the western site of southern South America with a peak in precipitation around latitudes 52°–53° S and generate arid conditions on the eastern side of the Andes (Garreaud et al., 2013). The SWW are persistent throughout the year with limited seasonal latitudinal variations (Garreaud et al., 2009). In austral winter (JJA), the SWW expand with a southerly position (~55°S) whereas it contracts in austral summer (DJF) in a northerly position (~50°S). During austral winters, the SWW extends, providing rainfall to central Chile (33°–40°

---

* Corresponding author.
E-mail address: nathalie.fagel@uliege.be (N. Fagel).

https://doi.org/10.1016/j.quascirev.2021.107134

S) (Markgraf, 1993; Garreaud, 2007). The SWW expansion is associated with a decrease of the wind velocity, especially in its core zone in southernmost Chile (50°–55° S) (Lamy et al. 2001, 2010). On the other hand, the wind speed increases in austral summer due to the contraction of the SWW (Garreaud et al., 2009).

Located within the mid-latitude 30–60°S belt, Patagonia is located between two main circulation systems, i.e. the Intertropical Convergence Zone (ITCZ) to the North and the Antarctic Convergence Zone (ACZ) to the South. Garreaud et al. (2013) emphasized that summer precipitation anomalies over Patagonia are correlated with Antarctic Oscillation (AAO) mode whereas winter anomalies are rather linked with El Niño-Southern Oscillation (ENSO)-controlled SWW anomalies over the SE Pacific (Montecinos and Aceituno, 2003).

For the last decades, paleoclimate studies in Patagonia emphasized high temporal climate variability over the late glacial (Gilli et al., 2005; Markgraf et al., 1992, 2013; Mayr et al., 2013; Moreno et al., 2001), the Holocene (e.g., Markgraf, 1993, 2003; Moreno et al., 2009; Moy et al., 2009, 2011; Villa-Martínez et al., 2012; Zolitschka et al., 2019) and the last millennium (e.g., Mayr et al., 2013; Moy et al., 2008; Sepulveda et al., 2009; Schimpf et al., 2011; Villalba, 1994). Among the main variability, precipitation variations, derived from different paleoclimate proxies (e.g., pollen and terrestrial indexes, charcoal content, magnetic susceptibility signal, mineralogical or geochemical ratios) and archives (e.g., marine or lacustrine sediments, ice cores, tree rings) were mainly used to reconstruct the evolution of SWW, in terms of wind intensity and latitudinal position over the Holocene (e.g., Villalba, 1994; Villa-Martínez and Moreno, 2007; Moy et al., 2008; Moreno et al., 2009; Lamy et al., 2010; Alvarez et al., 2015). According to vegetation distributions, divergent scenarios have been proposed for climate changes in Patagonia (44–49°S). Markgraf et al. (2003) suggested a northwards migration of SSW during the middle Holocene until they reached their modern position in the late Holocene (Markgraf et al., 1992). This latitudinal migration would be responsible for the Late Holocene higher climate variability in Patagonia (Markgraf et al., 2013). Villa-Martínez et al. (2012) rather suggested changes in the strength of the SWW at millennial and multi-millennial timescales since the last glaciation with no major latitudinal shifts.

For the last millennium however, the variability of the SWW remains less documented and poorly understood. It is particularly the case for the two major climate events, namely the Medieval Climate Anomaly (MCA) and the Little Ice Age (LIA) (e.g., Moy et al., 2008). The LIA was an apparently centuries-long climate state occurring around ca. 1400–1800 CE (Bradley et al., 2003) or 1300–1850 CE (Masson-Delmotte et al., 2013; Mann et al., 2009; Neukom et al., 2019). It contrasts with a warm temperature period ranging between 800 CE and 1200 CE, defined as the MCA (Neukom et al., 2019). In particular for those events, the strong variability revealed, for instance, in fjord sedimentary sequences from northwest Patagonia (Bertrand et al., 2014; Sepulveda et al., 2009) is inconsistent with paleoclimate reconstructions (Neukom et al., 2010). Those reconstructions display unequal and sparse proxy data distribution, especially for the Southern Hemisphere and for the last millennium (Neukom et al., 2010). Howeverr, paleoclimate reconstructions show poor coherency during these supposed cold and warm epochs over the past 2 kyr (Neukom et al., 2019). The LIA period, in particular, fails to present a spatio-temporal coherency with the coldest temperature ranging from the fifteen to the mid-nineteen century according to the site location. Inconsistent results have also been derived from the interpretation of different paleoclimate continental and marine Patagonian archives (Bertrand et al., 2014). As underlined by Moy et al. (2008), the scarcity of accurately-dated, continuous and unequivocally climate-related archives limit our understanding of recent and past Patagonian climate. In addition, the SWW fluctuations have mainly been studied in a latitudinal context, without taking account the influence of the Andes along a W-E longitudinal transect. Some interpretations of Westerlies fluctuations made on the western side of the Andes are indeed located in areas close to the eastern side generating contradictory results with previous studies (Lamy et al., 2010).

Therefore, this study aims to document environmental and climate variability, mainly related to the SWW influence, in a North Eastern Patagonian sector over the last millennium. The Lake Jeinimeni location provides a unique laminated record that contributes to better understanding the variability of SWW-related precipitation over the last centuries. Both sedimentological (i.e., varve thickness) and geochemical data (represented by the two first principal components) are correlated with local meteorological data (i.e., temperature, precipitation) to identify the main drivers of the sedimentation and further to follow their temporal evolution. The main scientific questions we would like to address in this manuscript are the following ones:

(1) Does the sediment record any correlation with any meteorological variable associated with the SWW-related precipitation?
(2) If any, how does it vary over the last millennium?
(3) Is any change in the sediment record associated with the manifestation of the MCA and the LIA in the region?
(4) Is the climate evolution deduced from Lake Jeinimeni record consistent with the paleoclimate records available on a regional scale?

2. Study area

The Lake Jeinimeni (latitude 46.5°S 72°0W, Fig. 1) is located in the Aysen XI region of Chile (Fig. 1A), at ~50 km south of Chile Chico (Fig. 1B), close to the border with Argentina. The geology of the Aysen region (Pankhurst et al., 1999) comprises three main units reported in Fig. 1C: 1) the Meso-Cenozoic North Patagonian batholith (hornblende–biotite granodiorites and tonalities); (2) the Devonian-Carboniferous Eastern Andean metamorphic complex (clastic metasediments) and; (3) the Late Jurassic Ibanez Formation (volcanic rocks, dacite and rhyolite, andesitic lavas and sedimentary intercalations). Some Eocene and Mio-Pliocene continental flood basalts and Pliocene granodiorites also outcrop South West of Chile Chico (De la Cruz et al., 2003). Quaternary alluvial and fluvio-glacial deposits with some intercalations of volcanoclastic deposits occur along the rivers. The topography of the Aysen area includes the southern extension of the Andean Cordillera, which is characterized by eternal snow, numerous glacial valleys and is covered by two major mountain ice fields (Glasser et al., 2008). Patagonian glaciers are highly sensitive to climate variability and have expanded and contracted several times during the Quaternary (Glasser et al., 2012). They react to latitudinal migrations of the SWW that control precipitation (Trenbeth, 1991; Lamy et al., 2010) and/or to temperature changes (e.g., Moreno et al., 2001; Heusser et al., 2006; Villa-Martínez et al., 2012). Major ice discharges are evidenced by moraine distributions at 1.1 Ma, 140–150 ka (MIS6), 16–23 ka (MIS2) (Hein et al., 2009). The Lago General Carrera/Buenos Aires is the regional largest moraine-damned lake (see Fig. 1B–Glasser et al., 2012). It was formed during the final glacier retreat (ca 12.8 ka), as the Patagonian Ice Sheet decoupled into the Northern and Southern Patagonian Ice Sheets and drainage routes opened up towards the Pacific Ocean (Turner et al., 2005).

Located at ~150 km East of the Northern ice field (altitude

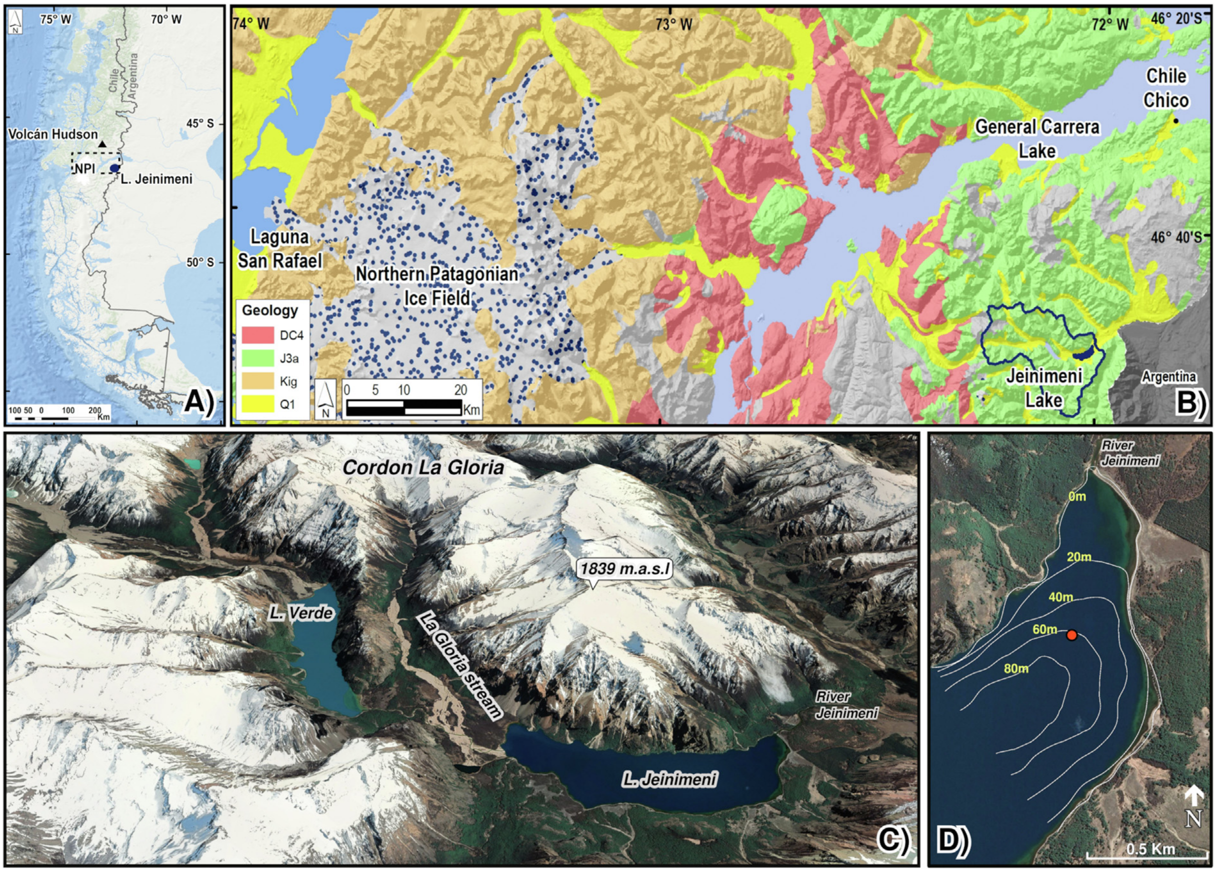

Fig. 1. (A) Location of Lake Jeinimeni within the Aysén region of Chile. The location of the Hudson volcano is reported on the map. (B) Simplified map of the regional geology, showing the North Patagonian batholith, the Eastern Andean metamorphic complex and the Late Jurassic volcano-sedimentary Ibañez Formation (Pankhurst et al., 1999). NPI: Northern Patagonian Ice Sheet, LGC/BA: Lago General Carrera/Buenos Aires. Lake Jeinimeni watershed is marked by a blue contour. (C) A lake watershed DEM (Digital Elevation Model) showing the main geomorphological features. The lake water body is reported in blue. (D) Map of basic bathymetric measurements and coring site, reported as a red dot, at the northern sector of Lake Jeinimeni. Images C and D, modified from Google Earth© 2019. (For interpretation of the references to color in this figure legend, the reader is referred to the Web version of this article.)

700–2500 m, ~4.000 km^2), the Lake Jeinimeni watershed (Fig. 1B) corresponds to a mountainous system with steep slopes and small foothills cut by rivers and numerous streams. The lake altitude is 840 masl and in terms of its dimensions has a surface area of 0.045 km^2, and the deepest point registered by this study was of 82 m. The Lake Jeinimeni with its narrow and elongated morphology belongs to the glacial Lago General Carrera/Buenos Aires watershed (Hein et al., 2010). Its origin is related to glacial outlet that allows the drainage of the Northern Patagonian icefield and is controlled by the bedrock topography (Glasser et al., 2008).

Present day climate of the Lake Jeinimeni watershed is cold and humid, with a steppe environment characterized by a sharp orographic eastward decrease in precipitation (e.g., Escobar et al., 1992). According to the closest meteorological station (i.e., Chile Chico station 46.58°S, 71.69°W, altitude 306 m, see location on Fig. 1B), the annual average temperature is low, it oscillates between 7 and 9 °C with a wide range between the coldest month (3 °C) and the warmest one (14 °C) (data reported in Corporación Nacional Forestal CONAF, 2017). Likewise, the annual precipitation is low (<500 mm; New et al., 2002). The Chile Chico reports a yearly average of cumulated precipitation of 293 mm ± 101 for the 1960–2014 interval (data from *Instituto de Investigaciones Agropecuarias* INIA - Hepp et al., 2018), with strong seasonal contrast between dry austral summer and wet austral winter. Such seasonal variability is mainly controlled by latitudinal migration and strength of the SWW. The measured wind velocity displays an annual average of 18 knots (7–25 knots) with a dominant W direction. The fastest wind speeds are observed during austral summer that are locally dry (data 2019 in Dirección General de Aeronáutica Civil DGAC, 2020). Located on the eastern side of the Andes, the austral winter precipitation in the Lake Jeinimeni area fall mainly as snow above 1000 m (Villalba et al., 1997). The accumulation of snow reaches up to 6–10 m each year. The Lake Jeinimeni is bordered by hills that are part of the called “Cordon La Gloria” (Fig. 1C), reaching altitudes above 1800 m. The main stream (i.e., La Gloria) that descends from the northwest carries a large amount of sediments that are deposited during spring in the valley between the Lake Verde and the Lake Jeinimeni. (Fig. 1C). These sediments can interrupt the flow of the Verde River, leading to a rise of the river and lake levels, eventually flooding the adjacent terranes (Henríquez and Alvear, 1987). The sedimentary transport is characterized by a strong seasonal control, evidenced by river discharge. Located at the outlet of the Lake Jeinimeni, the annual flow of the Jeinimeni River (Fig. 1D), measured monthly at the Chile Chico station since 2019 (data retrieved from Direccion General de Aguas - https://dga.mop.gob.cl/), displays a first increase related to precipitation in autumn (April–May), followed by a second one associated to snow melting in spring (Sept–Nov).

The vegetation is characterized by a steppe ecotone. The catchment (212 km^2) is covered by patches of Andean temperate deciduous forest leaded by *Nothofagus pumilio* and *Berberis ilicifolia* and temperate Mediterranean (so-called “Patagonian steppe” in

(Markgraf et al., 2007)) dominated by Poaceae herbs (*Fetusca pallescens*) and Apiacea (*Mulinum spinosum*) (Luebert and Pliscoff, 2006). The upper limit of the forest being located between 1200 and 1400 m, the low availability of vegetal cover up to the summit line favours erosion of the slopes and runoff (Corporación Nacional Forestal CONAF, 2017).

Due to the combination of young landscapes modelled by glacier and rivers and cool climate associated with the Northern Patagonia Ice Field, the soils in the study area are weakly developed, dominated by entisols on fluvial terraces, inceptisols on the surfaces exposed after ice retreat and some histosols (Pfeiffer et al., 2010). The study area is at the Southern limit of andisol development. Weakly developed in the River Baker drainage Basin (27 %, <0.6 m of volcanic cover), andisols are for instance absent south of the Lake General Carrera, in Chile Chico (Vandekerkhove et al., 2015). There is no evidence of active volcanism in the area that corresponds to the “Patagonian volcanic gap”. The closest active volcano (Hudson Volcano) is the southernmost volcano of the Southern Volcanic Zone (Stern, 2004), located 130 km to the north west of the study area. The ashes from the Hudson Quaternary explosive eruptions at 3.6 kyr BP and 6.7 kyr BP may have reached the study area (Naranjo and Stern, 1998) but according to Naranjo et al. (1993) recent eruptions in 1971 CE and 1991 did not deposit ash. In term of tectonic, Lake Jeinimeni is located at the south eastern side of the main structural strike-slip lineaments in North Patagonia (i.e., Liquiñe-Ofqui Fault Zone, Río Mañihuales Fault, Thomson, 2002), responsible for crustal intraplate earthquakes (Vanneste et al., 2018). However, an additional tectonic influence is possible since a fault crossing the lake was recently inferred by Encinas et al. (2018).

3. Material and methods

3.1. Sediment core

A 161 cm core (LJe14B, S46°50′42″, W72°00′47″) was taken in the eastern end of the lake (Fig. 1D), using an Uwitec® gravity corer at a water depth of 61 m in January 2014. A coring was attempted in a more distal site but it was not successful due to strong winds, frequent in austral summer.

The core was opened longitudinally and the archive half-core section was described and photographed. The sediment core is characterized by a fine sedimentary texture interrupted by several coarser layers named event and numbered from E1 to E8 according to increasing depth. As an exception the lowest part of the sediment core (155–161 cm) does not present any lamination. This section may be disturbed by coring and has not been further taken in account in the interpretation. The archive section was measured by non-destructive methods that include magnetic susceptibility, X-Ray imaging system (SCOPIX) and XRF core scaner. Magnetic susceptibility (MS) was measured with a Bartington® magnetic susceptibility meter MS2E point sensor with a 5 mm sampling interval. The working section was entirely subsampled utilizing aluminium boxes (25 cm length x 4 cm wide x 1.5 cm deep) that were slowly pushed into the cleaned sediment surface and was extruded with a knife, after a 180° rotation of the core section. The 25 cm long boxes were used to prepare the large thin section. The remaining sediment material was subsampled at 2.5 cm for loss-on-ignition (LOI) measurements.

3.2. Sedimentological and mineralogical analyses

C/N ratio were measured at 1 cm sampling resolution for the upper 15 cm then at 10 cm. (Lab. Oceanology and AGEs, Université de Liège). After a HCl pre-treatment to remove any carbonates, ~30 mg of sediment sample powder was analysed for C/N ratio and δ^{13}C with a Fisons® NA 1500NC elemental analyser coupled with an Optima IR-Mass Spectrometer (Hedges and Stern, 1984).

LOI was measured at 60 °C overnight for water content, at 550 °C for 4h organic matter and then at 950 °C for 2h for carbonates (following the technique described by Heiri et al., 2001).

X-ray diffraction (XRD) analyses were done at 5–10 cm sampling resolution. The sediment samples were dried at 40 °C and crushed with an agate mortar to 150 μm. The powder was transferred into a sample holder according to the backside method (Moore and Reynolds, 1997). XRD patterns were measured with a Bruker® D8- Advance Eco diffractometer (Copper Kα radiance, $\lambda = 1.5418$ Å, V = 40 KV, I = 25 mA) coupled with a linear Lynxeye Xe energy dispersive detector. The non-oriented powder was scanned from 2 to 70° 2θ with a step size of 0.009°2θ, and a time per step of 0.5 s. Semi-quantitative mineral abundance was estimated from the intensity of a diagnostic peak multiplied by a corrective factor defined by Cook et al. (1975) and Boski et al. (1998). The maximum intensity of the diffraction band at 4.04 Å was used to estimate the amorphous content in the sediments due to the occurrence of biogenic silica, volcanic glasses and/or organic matter (see more information in Fagel et al., 2017). The XRD mineralogy of the event layers was also done for comparison purposes with the background sediment.

In addition, the grain-size distribution was measured by a laser Malvern® Mastersizer 2000 diffraction particle analyser (Chemical Department, Université de Liège) on a selection of 8 samples from the coarse event layers evidenced by macroscopic description. The bulk sediment samples were sieved at 2 mm, dispersed in deionised water and introduced into the Hydro 2000G dispersion unit filled by 100 ml of water. The sample amount was adjusted to 15 % ± 5 of laser beam obscuration, homogenised and disaggregated with a 2000 rpm stirrer and 20 % of ultrasonic waves. The analysis was repeated at least 3 times to ensure the reproducibility of the analysis. The results are reported as frequency distribution curves (Sperazza et al., 2004).

Scanning Electron Microscope (SEM/EDX) and Electron Microprobe (EMPA) analyses have been performed on 2 coarser and darker layers (E1 and E2) observed in the upper 10 cm of LJe14B. The dried bulk sediment was sieved at 105–425 μm, then separated by liquid density separation using bromoform and the glass-rich light fraction was mounted in epoxy resin. SEM observations and EDX analyses were performed with a Quanta 650-F QEMSCAN (FEI) equipped with a Bruker 6\30 mm^2 EDX detector at the Aachen University (Germany). We used an acceleration voltage of 15 kV and a working distance of 10 mm. Photos were taken with a dwell time of 10 μs and EDX spectra were collected from 0 to 10 keV. Quantitative EMPA analyses of glass beads were performed with a Cameca SX 5 with 5 WDS spectrometers at the Ruhr-Universität Bochum (Germany). We used a beam with an acceleration voltage of 15 kV, a current of 8 nA and, for most analyses, a spot size of 10 μm. For EMPA calibration, the following standards were used for Kα X-ray: Na on albite, Mg on olivine-SC_233, Al, Si, K on orthoclase, Ca on wollastonite, P on apatite, Ti on rutile, Fe on hematite and Mn on rhodonite. The accuracy and reproducibility of the EMPA analyses were controlled by the repeated analyses ($n = 15$) of the international glass standard A99 (average sum of oxides 98.66 % ± 0.53).

3.3. Laminae counting and geochronological analyses

Sediment micro-structure was detailed by thin section observations under the microscope according to the procol described in Żarczyński et al. (2018). The sedimentary material was subsampled from the 25 cm-long aluminium boxes for large thin sections of 10–12.5 × 2 × 1.5 cm. The sediment was first shock-frozen in liquid nitrogen and, then freeze-dried at University of Liege. The next impregnation step with epoxy resin was done in specialized laboratories. Two 12.5 cm-long thin sections were produced for the upper 25 cm at EPOC, Univ. Bordeaux (France). Fifteen 10 cm-long (with 2 cm overlapping) were produced between 25 and 150 cm at MK factory in Potsdam (Germany).

All thin sections were scanned in polarized light with a resolution of 2400 DPI using a flatbed scanner and polarizing foils to identify, to count and to measure the thickness of the laminations. Axio Imager A2 (Zeiss, Germany) microscope was used to investigate thin sections under non-polarized and polarized light at the University of Gdanks.

After establishing a preliminary model of laminae succession representing annual sedimentation, couplets of laminae were counted on scanned images of thin sections. Counting was done twice by a single person for the whole sediment core with additional third counting restricted only to difficult core sections, in order to avoid possible misinterpretation. Finally, unclear couplets of laminae were included in the chronology as half a year and the counting uncertainty was increased by ±0.5 years, respectively. Following this step, the uncertainty was cumulatively summed along the chronology.

The age model was corroborated by applying ^{210}Pb, ^{226}Ra, ^{232}Th and ^{137}Cs data that were measured in the upper 16 cm of core LJe14b at EPOC (Univ. Bordeaux, France) using a low-background and high-efficiency well-type gamma detector. The analyses were performed on 1 cm-thick samples (~1.5 g of dried sediment) retrieved from the archive section. The excess ^{210}Pb ($^{210}Pb_{xs}$) activities were calculated as the difference of the measured ^{210}Pb and ^{226}Ra. Decrease with depth of $^{210}Pb_{xs}$ is then converted into age by applying the Constant Flux/Constant Sedimentation (CF/CS) model according to Appleby and Oldfield (1978).

In addition, radiocarbon dates were measured on 4 bulk sediment samples (Gliwice, Poland). They were calibrated by the Southern Hemisphere calibration curve SHCal13 (Hogg et al., 2013) and corrected by a reservoir age of 540 years estimated from the average C/N ratio of the core (16.7% at.) using the relationship established by Bertrand et al. (2012) for North Patagonian lakes. The Clam 2.2 code (Blaauw, 2010a, b) in the open source software R was used to perform an age-depth model by combining ^{137}Cs, excess ^{210}Pb and ^{14}C data.

3.4. Elemental core scanning

An X-Ray imaging system composed with an X-ray tube and a linear X-Ray camera has been used at the EPOC laboratory (Univ. De Bordeaux, France) to obtain an X-Ray image of the core, and grey-scale level of the sediment (data SCOPIX). Both measurements were performed on the archive half-core section. Sediment core scanning was done at a resolution of 2 mm an Avaatech XRF core scanner (Richter et al., 2006; Rothwell and Rack, 2006) equipped with a Rh tube on the Al boxes at the EPOC laboratory (Univ. Bordeaux, France). The XRF core scanning was done at 10, 30 and 50 KV and 15, 20 and 25s exposure time, respectively. Fifteen elements have been measured: Al, Si, S, K, Ca, Ti, Mn, Fe, Zn, Br, Rb, Sr, Y, Zr and Ba. Semi-quantitative concentration profiles of the elements are plotted along the sediment core based on the variations of their peak areas on the XRF core scanner spectra.

3.5. Statistic section

Geochemical elements obtained from XRF core scanner were analysed through Principal Component Analysis (PCA). PCA produces new sets of variables, called Principal Components (PCs) and only the PCs with eigenvalues >1 explain significantly the total variance of the dataset. Moreover, all the elements do not significantly contribute to the PCs and only those characterized by a communality values $\geq$ 0.5 are usually retained for PCA (Davis, 2002).

Geochemical data series are compared to monthly-averaged temperature and precipitation records from the local Chile Chico meteorological station, which began reporting in 1960 CE (Hepp et al., 2018). The calibration time window was extend down to 1930 CE by using the climate reconstruction CRU_TS 4.03 (Harris and Jones, 2020), retrieved for the geographical coordinates 47°.00–46.40° latitude S and 72.20–71.51° longitude W (http://climexp.knmi.nl). The retained calibration interval spans from 1930 CE to 1988 CE. The oldest CRU_TS 4.03 data for 1900–1930 CE interval was not retained for calibration since Elbert et al. (2012) have emphasized before 1930 CE a poor quality of the reanalysis in the area. The youngest interval 1991–2014 AD, corresponding to the upper 5 cm of LJe14B record, has not been take into consideration due to the presence of a coarse event E1 (4.5–5 cm). Below the E1 event, the LJe14 data were linearly interpolated in order to compare the core proxies with yearly-averaged meteorological data. For the comparison of meteorological data and sedimentological proxies, we applied moving average filters of three, five and seven-years for the period 1930–1988 AD.

Pearson coefficients and p value ($p < 0.05$) were used to evaluate the strength of the relationships for determining the main environmental controlling factors. All statistical analyses were performed in R (R Development Core Team, 2016) using the *psych* and *corrplot* packages (Revelle, 2017; Wei and Simko, 2017).

4. Results

4.1. Core sedimentology and mineralogy

The core image, grey-scale level (SCOPIX), Al count (XRF core scanner), magnetic susceptibility, water and organic matter contents (LOI60 and LOI550, respectively) and geochemistry of organic matter (C/N and δ^{13}C) measured on the core LJe14B are presented in Fig. 2. The sediments retrieved in core LJe14B are mainly detrital and inorganic, with a water content ranging between 11 and 43 % (average 34 ± 6 %) and an averaged organic matter abundance of 1.6 ± 0.3 % (1.3 < LOI at 550 °C < 4.2 %) (Fig. 2). The sediments of Lake Jeinimeni are made by finely laminated light brown clayey silt (fine silt mode at 3 μm) with a few remarkable layers, referred to event layer (E) and described in the next section. C/N and δ^{13}C values are relatively constant, with averages of 16.7 ± 3.8 (atomic ratio) and −26.2 ± 0.4 ‰, respectively. The average high C/N ratio indicates an important contribution of reworked organic matter from the watershed (Meyers and Teranes, 2001). Sparse benthic diatoms are observed in the thin sections, with *Eunotia*, *Cymbella*, *Nitzschia*, *Encyonema* and *Rhopalodia* as the main representative genera. Central planktonic frustules are also detected in the upper part of the core (4–6 cm). Diatoms represent an estimated abundance <1 %, they are indicative of a marshy-like environment (I. Israde Alcantara**,** personal communication 2/2019).

The mineralogical assemblages of core LJe14B are quite constant through the core (SM Fig. 1). Clay minerals (36 ± 4 %) and quartz (31 ± 3 %) are the dominant phases, associated with similar abundance of K-feldspars (13 ± 3 %) and plagioclase (12 ± 2 %), mica (8 ± 1 %) and traces of chlorite and amphibole (<2 %). The total amorphous phases average 11.8 ± 1.9 % of the core mineralogy, with a maximum of 16 % in the two tephra layers. It is made by organic matter content (1.3–4.2 %), diatoms (~1 %), tephra glasses at 4.5–5 cm and 7–7.5 cm and reworked volcanic material from the watershed.

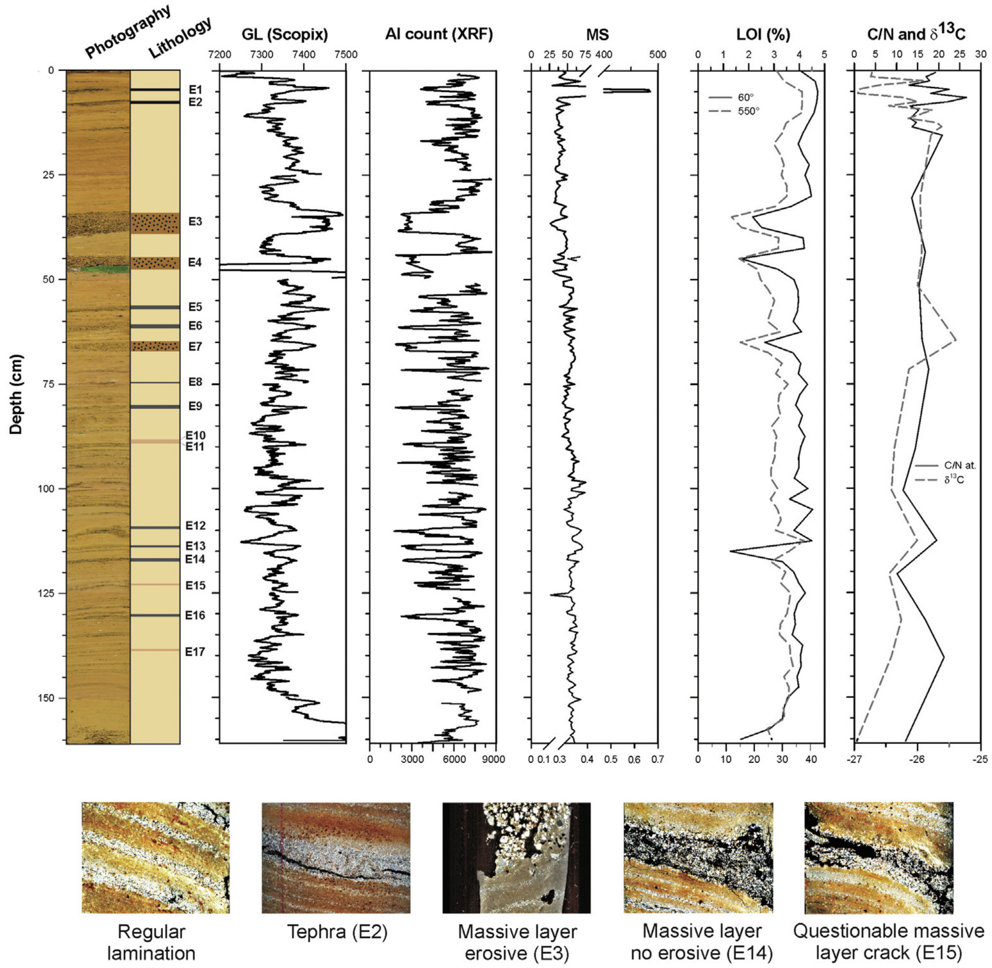

Fig. 2. Core image, simplified lithological column with the event layers depths and major measurements, which include: GL = X-ray grayscale, Al counts, MS = magnetic susceptibility, water (LOI60) and organic matter content (LOI550), carbon/nitrogen atomic ratio (C/N) and carbon stable isotope (δ^{13}C) measurements of core LJe14B. The simplified lithological column indicates the positions of 17 event layers, noted E1 to E17, which interrupt the background sedimentation. The three types of events are plotted with different symbols: the thickest and coarsest layers with erosive base in brown; the coarse layers without any erosion in black; the questionable layer resulting from cracks and sediment deformation in pale brown. E1 at 4.5–5 cm and E2 at 7.4–7.9 cm correspond to two tephras layers. B) Images illustrating the background sedimentation and different event types. The scale of each picture is approx. 20 mm. Note the reported MS curve represents an average of three profiles. (For interpretation of the references to color in this figure legend, the reader is referred to the Web version of this article.)

4.2. *Laminated sediments*

The sedimentary sequence of Lake Jeinimeni in core LJe14B is made by millimetre-scale rhythmic alternations of coarse grained quartz- and feldspar-rich layers and fine grained clayey silt layers with minor organic contributions. This laminated pattern resembles clastic varves with typical particle-size differences between coarse- and fine-grained laminae deposited during spring/summer snowmelt and winter calm conditions, respectively (Sturm, 1979).

The preservation quality of laminations is generally good except the sections adjacent to the event layers, where disturbances in the sediment structure appear. The base of coarse grained laminae forms sharp boundary with underlying fine grained laminae. In contrast, the contact between coarse grained and overlying fine-grained laminae is gradual and does not form a distinct boundary. Instead, a smooth fining upward is visible, which makes a reliable measurement of individual laminae (coarse *vs.* fine) thickness impossible. Thickness of laminae couplets ranges from 0.3 to 7.6 mm, although the majority (80 %) is in the range 0.7–2.5 mm. The averaged thickness for the entire sediment sequence is 1.54 ± 0.89 mm.

4.3. *Event layers*

In the upper part of the core, two darker event layers are evidenced by naked eye at 4.5–5 cm and 7.4–7.9 cm (i.e., E1 and E2, respectively) and well-marked under the microscope by sharp bases with no or minimal erosion (Fig. 2). The uppermost layer displays the highest measured magnetic susceptibility value in the core (i.e., 486 SI, in contrast with the core average of 54 ± 36 SI). The samples at depths of 4–5 cm and 7–8 cm are dominated by silt (69 %), yet are associated with 12–17 % of sand and 14–18 % of clay. They both present a fine silt mode (8.5–9.8 μm), darker grey-scale values and lower Al count (Fig. 2). Similar drops are observed in the Si, K and Rb core profile whereas Ti, Ca and Sr rather display a marked increase only at 4.5–5 cm (Fig. 1 and SM Fig. 2). Only the Zr profile evidences a second increase at 7–7.5 cm (SM Fig. 2). The presence of glass shards was further confirmed by SEM observation and EDX analyses on both E1 and E2 samples (Fig. 3). In addition, the EMPA major geochemistry of the glass shards from E1 corresponds to an andesite with a high K content (averaged abundance

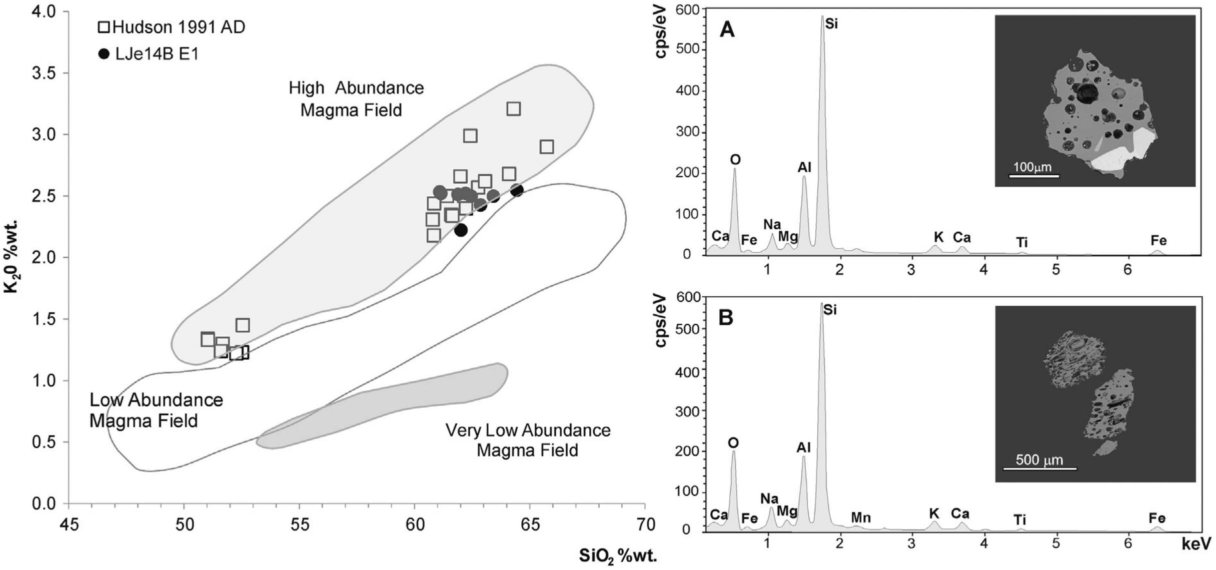

Fig. 3. On the left panel, Electron Microprobe (EMPA) characterisation of glass shards extracted from E1 and E2 event layers in core LJe14B. All the analysed glasses fit with the field of the High Abundance Magma Field of the eruptive products from the Southern Volcanic Zone (SVZ) as reported in Stern et al. (2015). Moreover, the glass chemistry is consistent with the signature of the Hudson 1991 eruption (data from (Naranjo and Stern, 2004). On the right panel, Scanning Electron Microscope photographs and elemental EDX composition of representative glassy samples with circular or elongated gas bubbles: A. E1 4.5–5 cm, B - E2 7.4–7.9 cm. The EDX major chemistry of the observed glasses from both E1 and E2 layer is consistent with a plagioclase composition.

of $SiO_2 = 62.39$ wt% ± 1.07, $K_2O = 2.48$ wt% ± 0.10, n = 9).

Between 34 and 67 cm, three pluri-centimetre event layers interrupt the laminated sedimentation: E3 from 34 to 38 cm, E4 from 44 to 48 cm and E7 between 65 and 67 cm (Fig. 2). They are characterized by an irregular erosive base and a thinning upward graded bedding. Their grain-size corresponds to fine to medium sand with some gravels. According to the classification of Folk and Ward (1957) they are poorly to very poorly sorted, with sorting values ranging between 1.8 and 3. Samples 35–36 cm and 65–66 cm are made by > 82 % of sand associated with 14 % of silt and 4 % of clay, with a mode at 307 and 184 µm, respectively. Those layers are characterized by darker colour, a marked decrease in Al count and porosity, slightly lower magnetic susceptibility, lower water content and organic matter but no change in the C/N nor $\delta^{13}C$ values (Fig. 2). The sample 44–45 cm presents a mode at 178 µm with 32 % of sand, 46 % of silt and 22 % of clay particles (SM Fig. 3). Note there is no significant difference in the mineral abundance of the event layers E3, E4 and E7 by comparison with the background sediment (SM Fig. 1).

In addition to the two pluri-millimetric E1 and E2 and the three pluri-centimetre layers E3, E4 and E7, twelve additional remarkable event layers have been observed under the microscope within the 150 cm of LJe14B (Fig. 2). They correspond to two groups identified on the thin sections: (1) non-erosive or representing minimal erosion only, and (2) layers of deformed laminations and cracks. First group is represented by eight thin (4–11 mm) layers with no or only minimal erosion (E5, E6, E8, E9, E12, E13, E14, E16). Low potential erosion was estimated based on the contact with underlying laminae, which were not disturbed. Second group consists of four layers (E10, E11, E15, E17), which partly result from cracks and sediment deformations. It is difficult to interpret unambiguously if these layers are original sedimentation structures or artefacts related to sediment impregnation.

4.4. Core chronology

For the upper section of core LJe14B (0–16 cm), the age model was derived from $^{210}Pb_{xs}$ and ^{137}Cs data (Fig. 4a, data reported in Table 1). The profile of $^{210}Pb_{xs}$ displays drastic variations with low $^{210}Pb_{xs}$ level in the uppermost 4 cm (Fig. 4b). Such low activity of ^{210}Pb in the first centimeters could be related to rapid sedimentation event, that dilutes $^{210}Pb_{xs}$ (e.g., Quiroz et al., 2005). This hypothesis is consistent with the occurrence of E1 event observed at 4.5–5 cm in LJe14B. Only the samples characterized by equivalent ^{232}Th activities (~70 mBq/g) are retained (Table 1). This long-lived radionuclide is associated with the detrital fraction and then equivalent activities may indicate of rather equivalent lithological sources or proportions. The sample at 7–8 cm was discarded from the age model: this level was only measured to precise the shape of the ^{137}Cs peak, and the counting session was not long enough to allow a reliable determination of $^{210}Pb_x$ (low ^{229}Th for event E2). The control points are: 1) the surface age (2013 AD) and; 2) the maximum ^{137}Cs activity (20 mBq/g) observed at 8.5 cm (Fig. 4b) and associated to the most intense period of atmospheric nuclear tests fallout (Stupar et al., 2014). The ^{137}Cs peak is fixed at 1965 AD ± 5 yr.

For the upper 16 cm, ages were calculated every 2 mm with 95 % confidence ranges assuming a linear regression (Fig. 4a). The Pb–Cs age model gives a mean sedimentation rate of 1.43 mm/yr for the upper 15.5 cm of core LJe14B. This value is fully consistent with the average thickness of laminae couplets of 1.48 ± 0.86 mm measured for the same depth interval. Moreover, there is a good consistency between laminae couplets counting and the $^{210}Pb/^{137}Cs$ age model (Fig. 4a). Assuming an annual sedimentation, the chronology based on varve-counting is reported for the whole core in Fig. 4c. Scanned images of the thin sections were correlated with core photographs to identify gaps in the thin sections and further refine the proposed age model. In Lake Jeinimeni the uppermost 150 cm sedimentary sequence recovered in core LJe14B encompasses 759 ± 62 years (i.e., error of 8 %), from 2013 down to 1254 AD (1193 AD < age < 1318 AD), without taking account 15 cm of cumulative events (E1 to E17). The sedimentary sequence may be uncompleted due to the erosive action of the pluri-centimetre massive deposits, especially E4 and in a lesser proportion E3 and E7.

For the lower part of the core, only bulk sediment was available

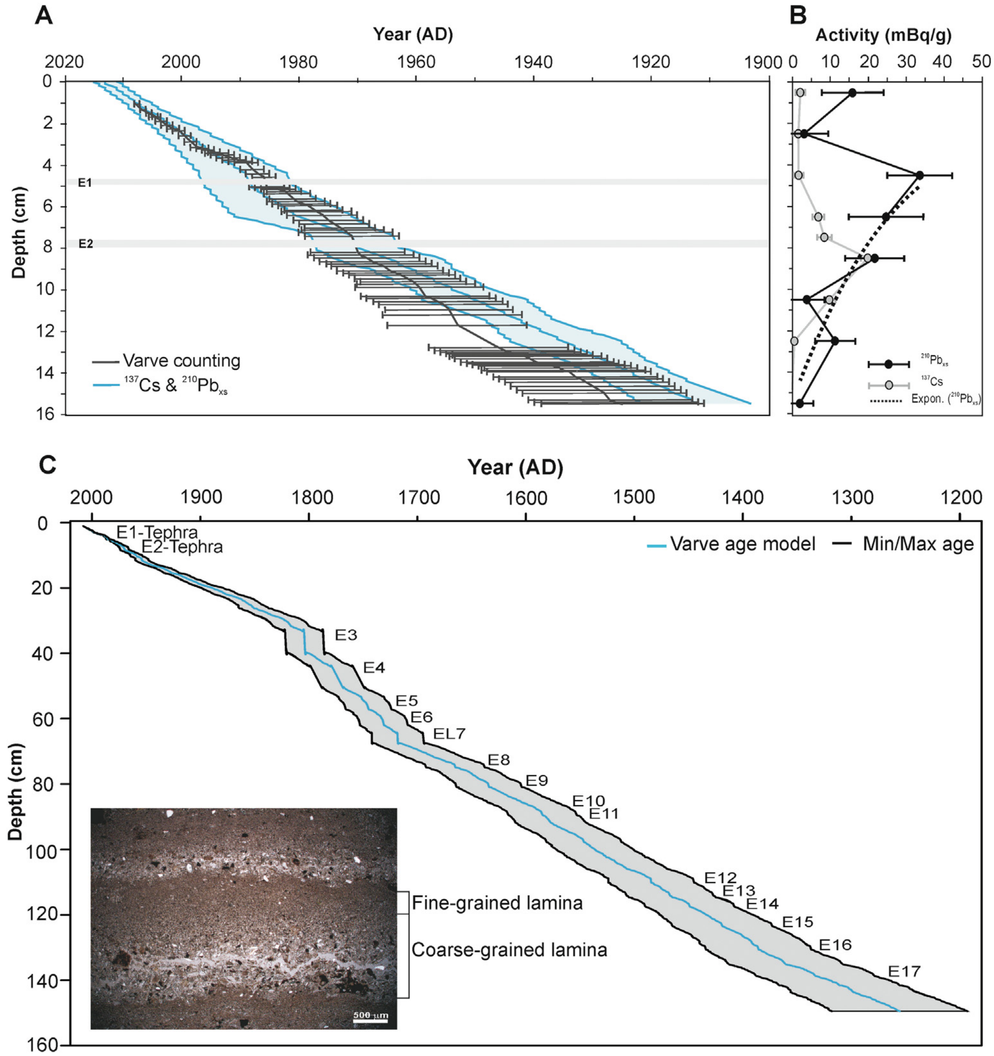

Fig. 4. Age model for the upper 16 cm of core LJe14B. A. Comparison between the age-depth model derived from varve counting and its uncertainty reported as black lines and the age-depth model based on ^{137}Cs and excess ^{210}Pb data and its uncertainty marked as blue lines. For varve counting, maximum age takes in account all varves, minimum age does not include uncertain varves and mean age represents the half of uncertain varves added to chronology. The grey bars indicate events E1 and E2 correspond to the two Hudson eruptions of 1991 and 1971 AD, respectively. B. The curve corresponds to the exponential fit of the ^{210}Pb$_{xs}$ decrease. Note the two uppermost samples (0–1 cm and 2–3 cm) and the sample at 7–8 cm (tephra E2) were excluded from the age model since they present no or low ^{210}Pb$_{xs}$. The age model derived from ^{137}Cs and excess ^{210}Pb activities (B) is elaborated by linear interpolation with Clam 2.2 code (Blaauw 2010a,b). C. Age model for core LJe14B as derived from varve counting. The events labelled E1 to E17 are marked. The enclosed photo gives an example of the laminated sediment texture, with an alternation of thicker quartz and feldspar-rich coarse-grained lamina and thinner fine-grained lamina. (For interpretation of the references to color in this figure legend, the reader is referred to the Web version of this article.)

Table 1
Measured activities of ^{210}Pb$_{xs}$, ^{232}Th and ^{137}Cs in sediment samples of the uppermost 16 cm of core LJe14B.

Sample	210Pbxs	–	–	232Th	–	–	137Cs	–	–
cm	mBq/g			mBq/g			mBq/g		
0–1	16	±	8	65	±	2	2.1	±	0.8
2–3	3	±	6	77	±	2	1.6	±	0.6
4–5	34	±	9	58	±	2	1.7	±	0.7
6–7	25	±	10	69	±	2	6.9	±	1.0
7–8	n.d.	–	–	73	±	2	8.5	±	0.9
8–9	22	±	8	67	±	2	19.9	±	1.0
10–11	4	±	5	73	±	1	9.8	±	1.0
12–13	11	±	5	75	±	1	0.6	±	1.0
15–16	2	±	4	69	±	1	−0.6	±	0.0

for radiocarbon dating as no terrestrial macroremain was found to be dated. Even taking account the reservoir correction established for the same Patagonian sector (Bertrand et al., 2012), the calibrated radiocarbon dates remain quite old (Table 2) and induce a sharp drop of the sedimentation rate between the upper part of the core (0.16 cm/yr) and the lower part of the core (0.03 cm/yr) (see SM Fig. 4). As such change was not supported by any lithological observation, the bulk sediment dates were discarded from the age model. Lacustrine bulk sediments may be contaminated by old “dead” carbon from the watershed (e.g., Abbott and Stafford, 1996; Moy et al., 2011; Albéric et al., 2016).

5. Discussion

5.1. Annual character of the sedimentation

A set of observations attests for the annual character of the sedimentation retrieved in the core LJe14B. First, the annual character of the laminations is supported by a calculated significant

Table 2
AMS radiocarbon ages obtained on bulk sediment samples. An age reservoir correction of 540 years was applied taking in account a C/N ratio of 16.7 (% at.) following the equation proposed by Bertrand et al. (2012). Four intervals (4.5–4.9, 34–39 cm, 44–48 cm, 65–67 cm) were considered as events and were removed for the calibration. Radiocarbon dates were calibrated by Clam calibration program (Blaauw et al., 2010a,b) using atmospheric SHCal13 calibration curve (Hogg et al., 2013). Samples were measured at the Gadam Radiocarbon Laboratory.

Sediment core depth (cm)	Lab. Nb.	Age 14C (BP)	Calibrated age (yr AD/BC)		Prob. (%)
			min	max	
LJe14B/32-33	GdA-5041	1525 ± 20	1034	1152	95
LJe14B/53-54	GdA-4038	3389 ± 29	−1050	−890	89.8
			−880	−846	5.1
LJe14B/95-96	GdA-4039	3158 ± 28	−813	−747	69.9
			−685	−667	6.1
			−642	−554	18.9
LJe14B/155-156	GdA-4040	3655 ± 31	−1420	−1257	90.6
			−1252	−1231	4.2

An age reservoir correction of 540 years was applied taking into account a C/N ratio of 16.7 (% at.) following the equation proposed by Bertrand et al. (2012). Four intervals (4.5–4.9, 34–39 cm, 44–48 cm, 65–67 cm) were considered as events and were removed for the calibration. Radiocarbon dates were calibrated by Clam calibration program (Blaauw et al. 2010a,b) using atmospheric SHCal13 calibration curve (Hogg et al., 2013). Samples were measured at the Gadam Radiocarbon Laboratory.

correlation between the measured varve thickness and local meteorological data. The highest Pearson coefficient of −0.71 ($p < 0.0001$, Table 4) is obtained between austral spring (SON) precipitation and varve thickness. The coefficient is moderate but still significant between annual precipitation and varve thickness (−0.53, $p < 0.0001$ - Table 4). The correlation is attested for the last century, i.e., from 1930 CE and 1988.

Second, the number of laminae couplets observed on the thin section within the upper 16 cm of the LJe14B core is consistent with the $^{210}\mathrm{Pb}/^{137}\mathrm{Cs}$ age model (Fig. 4a). This observation confirmed the annual character of the deposits at least for the upper core section, i.e, for the last 120 years corresponding to the age window covered by the $^{210}\mathrm{Pb}$ geochronometer.

A third argument is related to the calculated age of the two event layers observed in the uppermost 8 cm of core LJe14B. The $^{210}\mathrm{Pb}/^{137}\mathrm{Cs}$ age model gives an age of 1981–1996 CE for the event layer E1 and 1963–1977 for event E2. Given by Clam interpolation, the *best ages* of 1988 CE and 1970 CE for E1 and E2, respectively, are very close to the age of the two most recent explosive eruptions of the Hudson volcano (i.e., HU 1991 AD and HU 1971 AD, (Scasso and Carey, 2005)). The activity of the Hudson volcano started at ~1 Ma (Orihashi et al., 2004) and the Holocene stratigraphy of its fallout deposits records at least twelve more explosive eruptions. Among them the most important eruption happened in August 1991 CE (Naranjo and Stern, 1998). Another historical eruption took place in August 1971 CE, when an eruptive column rose 14 km high, leaving a wide scale tephra fall out deposit over the region (Fuenzalida, 1976). In addition to the age consistency, the glass shards-rich content detected by SEM observations of the E1 and E2 samples (Fig. 3) confirm their volcanic origin. The microprobe analyses of the glass shards of the sample 4–5 cm gives a chemical composition similar to the signature of the Hudson eruptions, in particular with the 1991 CE eruption (Naranjo and Stern, 1998) (Fig. 3).

Since the laminae couplets display the same structure under the microscope all along the core LJe14B depth, we assume that the sedimentary deposition in the lower part of the core also represents an annual character and are therefore interpreted as varves.

Table 3
Results of principal component analysis (PCA) on raw XRF core scanner dataset. The table gives the contribution of each principal component in total variance. PCA was performed first with all elements, second without Mn because its communality value was lower than 0.5.

Total Variance Explained						
Component	All elements			Mn excluded		
	Initial Eigenvalues			Initial Eigenvalues		
	Total	Variance %	Cumulative %	Total	Variance %	Cumulative %
1	6.01	40.0	40.0	5.94	42.4	42.4
2	2.09	13.9	53.9	2.07	14.8	57.2
3	1.28	8.6	62.5	1.27	9.1	66.3
4	1.16	7.8	70.3	1.16	8.3	74.6
Elements	Communalities					
Al	0.90			0.90		
Si	0.87			0.86		
K	0.94			0.94		
Ti	0.80			0.82		
Fe	0.84			0.84		
Ca	0.86			0.85		
Sr	0.79			0.81		
Y	0.56			0.56		
S	0.54			0.55		
Br	0.50			0.54		
Zn	0.54			0.50		
Rb	0.84			0.84		
Zr	0.70			0.76		
Mn	0.19			–		
Ba	0.66			0.67		

Table 4
Calibration of varve thickness and geochemical data (principal components PC1 and PC2, Si/Al) with CRU-TS reconstruction over 1930–1988 AD. Meteorological data retrieved from (National Center for Atmospheric Research Staff, 2017) Statistically significant correlations, according to Pearson's correlation coefficient with p-value < 0.05, are reported in color (positive in red, negative in blue). The number of asterisks gives the degree of significance: *p < 0.01, **p < 0.001 and ***p < 0.0001. Note the same correlations are observed for averaged or accumulated precipitation.

Interval (years AD)	1930–1988																
Number of data	58 (without tephra 1971)				56 (without tephra 1971)				54 (without tephra 1971)				52 (without tephra 1971)				
Moving average	None, raw data				period of 3 years				period of 5 years				period of 7 years				
Geochemical proxy	Varve	PC1	PC2	Si/Al	Varve	PC1	PC2	Si/Al	Varve	PC1	PC2	Si/Al	Varve	PC1	PC2	Si/Al	
Averaged temperature (°C)	Annual	0.18	0.09	0.03	0.02	0.18	0.07	0.04	0.00	0.08	0.08	0.01	−0.01	−0.03	0.14	0.18	−0.01
	DJF	0.11	0.09	−0.15	−0.17	0.18	0.04	−0.18	−0.25	0.07	0.06	−0.18	−0.28	0.01	0.11	−0.17	−0.30
	MAM	0.03	0.18	0.00	−0.03	0.16	0.27	0.15	0.09	0.11	0.35	0.24	0.21	0.01	0.43**	0.43*	0.24
	JJA	0.07	−0.17	0.09	0.32	−0.05	−0.3	−0.03	0.40 **	−0.15	−0.47***	−0.08	0.49**	−0.27	−0.54***	−0.18	0.50**
	SON	0.2	0.14	0.14	−0.13	0.06	0.2	0.29	−0.28	0.13	0.23	0.49**	−0.35	0.24	0.24	0.58***	−0.39*
Averaged precipitation (mm)	Annual	−0.19	−0.08	−0.18	0.41 **	−0.25	−0.08	−0.29	0.55***	−0.43*	−0.17	−0.34	0.64***	−0.53***	−0.25	−0.31	0.72***
	DJF	−0.1	−0.07	−0.16	0.04	−0.06	−0.09	−0.33	0.06	0.01	−0.2	−0.38*	0.15	0.03	−0.34	−0.43*	0.22
	MAM	−0.14	−0.07	−0.20	0.39	−0.19	−0.11	−0.22	0.60***	−0.48**	−0.18	−0.27	0.66***	−0.61***	−0.28	−0.25	0.75***
	JJA	−0.16	−0.01	0.02	0.36	−0.19	−0.02	−0.08	0.44***	−0.21	−0.03	−0.14	0.48**	−0.24	−0.02	−0.09	0.49**
	SON	−0.05	−0.06	−0.17	0.11	−0.21	−0.04	−0.30	0.25	−0.54***	−0.17	−0.34	0.44**	−0.71***	−0.29	−0.35	0.58***
Accumulated precipitation (mm)	Annual	−0.19	−0.08	−0.18	0.41 **	−0.25	−0.08	−0.29	0.55***	−0.43*	−0.17	−0.34	0.64***	−0.53***	−0.25	−0.31	0.72***
	DJF	−0.1	−0.07	−0.16	0.04	−0.06	−0.09	−0.33	0.06	0.01	−0.2	−0.38	0.15	0.03	−0.34	−0.43*	0.22
	MAM	−0.14	−0.07	−0.20	0.39	−0.19	−0.11	−0.22	0.60***	−0.48**	−0.18	−0.27	0.66***	−0.61***	−0.28	−0.25	0.75***
	JJA	−0.16	−0.01	0.02	0.36	−0.19	−0.02	−0.08	0.44***	−0.21	−0.03	−0.14	0.48**	−0.24	−0.02	−0.09	0.49**
	SON	−0.05	−0.06	−0.17	0.11	−0.21	−0.04	−0.30	0.25	−0.54***	−0.17	−0.34	0.44**	−0.71***	−0.29	−0.35	0.58***
Geochemical proxy	Varve	1	0.17	−0.04	−0.19	1	0.34*	−0.02	−0.31	1	0.45**	0.07	−0.39*	1	0.54***	0.15	−0.47**
	PC1		1	0.16	−0.12		1	0.23	−0.11		1	0.39	−0.11		1	0.56	−0.15
	PC2			1	0.09			1	0.00			1	−0.08			1	−0.16
	Si/Al				1				1				1				1

5.2. Sedimentary deposit conditions

Lake Jeinimeni sediments are mostly clastic with a very minor biogenic component. The organic matter content is relatively low, ranging between 1.3 and 4.2 % (Fig. 2). Its geochemical signature, with high C/N (mean 16.7 ± 3.8 atomic ratio) and very negative δ^{13}C values (−26.96 to −25.39), reflects a mixing of lacustrine and terrestrial organic matter (Meyers and Teranes, 2001). The stable mineralogical assemblages suggest that the source of detrital supplies remains constant through time. However, changes in grain-size, observed at both microscopic and macroscopic scales, reflect different modes of sediment transportation.

The elemental data measured on core LJe14B allows to explain in further detail the sedimentation pattern (see Davies et al., 2015 for a review). In the following section the PCA scores of the main PCs (PC1, PC2) will be reported along core depth to track for lacustrine environmental variability. Among the XRF core scanner dataset, some elements (e.g., Al, Si, K, Ti and Fe) display similar trends (Fig. 2 and SM Fig. 2), and by applying a multivariate statistical analysis such as Principal Component Analysis (PCA), it is possible to disentangle the forcing mechanisms behind the temporal variability (e.g., Avşar et al., 2014). Four Principal Components (PC) were identified representing 70.3 % of the total variance (Table 3). However, according to the communality values, the contribution of Mn (0.19) is lower than the other elements and was therefore removed from the analysis. After its exclusion, the four PCs explain 74.6 % of the total variance, with 42.4 % of the variance explained by PC1 and 14.8 % by PC2 (Table 3). PC1 is positively correlated with Al, Si, K, Ti, Fe, Ca, Sr and Y and negatively associated with S, Zn and Ba. Among these elements, Al, Si, K, Ti, Fe are indicators of detrital supplies. Abundant in clay minerals, micas and feldspars, they correspond to lithogenic elements, geochemically stable, hosted by resistant minerals with a conservative behaviour through the sedimentary cycle (Boës et al., 2011). In addition to their affinity for carbonates, Ca and Sr are also present in the detrital sedimentary fraction, mainly in plagioclase minerals. S is often associated to organic matter (e.g., Avşar et al., 2014) that may also include metallic element like Zn. PC2 explained the 14.8 % of the variance and is positively associated with Sr, Ca and negatively with Rb, Ba. In addition to biogenic component, Sr and Ca are also present in detrital fraction mainly present in plagioclase feldspars (Davies et al., 2015, p. 196; Rothwell and Croudace, 2015, p. 63). Rb is chemically similar to K that it substitutes in K-feldspars and micas (Davies et al., 2015, p. 196; Rothwell and Croudace, 2015, p. 81), two minerals less easily chemically-weathered than plagioclase. Rb is rather enriched in fine clay and silt fraction (Kylander et al., 2011). In the PCA results, Ba is distributed in close proportion between PC1 and PC2. According to its ionic ratio, Ba may substitute Ca and Sr in plagioclase, but also K in K-feldspars [e.g., in sanidine - cf. Cherniak (2002), Puchelt (1969−1978) cited in Rothwell and Croudace (2015), page 79].

The measured elements by the XRF provide hints about the sediment lithologies (i.e. tephra, fine clayey silt, fine to medium sand, coarse sand with some gravels). In the binary diagram PC1 *vs.* PC2 (Fig. 5), most samples are clustered along the PC1 axis and are distributed in three groups characterized by different grain sizes: (1) the highest positive values of PC1 fit with the field of the fine clay-rich samples; (2) the moderate negative PC1 values range within the field of the coarse sandy-rich samples; (3) the more negative PC1 values mainly correspond to the field of the three pluri-centimetre thick event layers E. Such sample distribution suggests that PC1 is sensitive to the hydrodynamics of the aquatic system, notably the energy of hydrodynamics . All the elements associated to the PC1 have a detrital origin delivered by soils reworking and/or watershed erosion of the parental sediments and rocks. The river transports fine detrital-rich supplies that settle down at the coring site during calm conditions whereas coarser material is transported during periods of higher energy hydrodynamics. In addition to this main trend observed along PC1 axis, a few samples are rather aligned along the PC2 axis. These samples correspond to the tephra layers (i.e., events E1 and E2) observed in the upper core section and some type of detrital interference by them (i.e., labelled as tephra-influenced layer on Fig. 5). In the PC1-PC2 biplot, the distribution of Sr and Ca (and Zr in a lesser proportion) may be influenced by the tephra layers. Such observation is consistent with the results of Unkel et al. (2010) who evidenced enrichment in Zr associated to Ca, K, Ti and Sr in a Hudson volcano-related tephra layer from Laguna Cascada in South Chile.

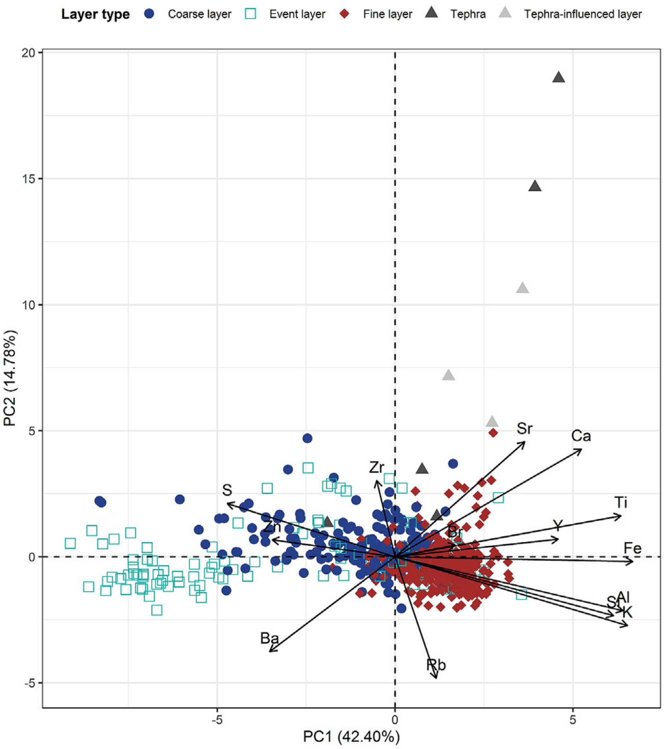

Fig. 5. PCA biplot of XRF core scanner dataset (except Mn) reported as a binary diagram of the first two principle components PC1 and PC2. The samples are reported with different symbols according to their dominant lithology. This diagram emphasizes the distribution of the samples in 4 groups according to their lithology. The three groups distributed along the PC1 axis correspond to sedimentary samples dominated by fine-grained lamina (red diamond), coarse-grained lamina (blue circle), and the massive, sandy to gravely, event E3, E4 and E7 (open blue square). The fourth group plots along the PC2 axis and corresponds to the tephra (dark grey triangle) and tephra-influenced (light grey triangle) layer. (For interpretation of the references to color in this figure legend, the reader is referred to the Web version of this article.)

Concerning the thick sandy to gravely event layers, similar coarse fining upward sedimentary deposits with an erosive base are often interpreted as resulting from floods deposited by hyperpycnal flows (e.g., Chapron et al., 2006). According to Mulder et al. (1998), the critical suspended-sediment concentration needed to produce a hyperpycnal plume in a lake is quite low and may result by river discharge into the lake. Among the event units observed in LJe14B, those layers with an erosive base (i.e. E3, E4 and E7) most probably record large flood-triggered turbidites. Only the upper sequence deposited during the falling limb of the flood is preserved, their basal coarsening upward sequence corresponding to the waxing flow being erased due to strong erosion (e.g., Gyuard et al., 2007). In LJe14B, the event units are irregularly distributed over core depth, most of them being observed between 34 and

67 cm depth (Fig. 6). In particular, the event layers characterized by erosive bases may be triggered by different climate-related mechanisms (e.g., stormy winter conditions - Jenny et al., 2002 and/or exceptional snowmelt events, heavy rains, catastrophic drainage - Gyuard et al., 2007) or tectonic-related mechanisms (e.g., slumps, earthquakes - Siegenthaler and Sturm, 1991; Waldmann et al., 2011, Moernauts et al., 2018). The climate-driven mechanism is the most probable as Lake Jeinimeni is located at the south eastern side of the influence area of the Liquiñe-Ofqui Fault Zone (Thomson, 2002).

5.3. Meteorological calibration

The local instrumental data from Chile Chico station display a significant high correlation with CRU_TS precipitation ($R^2_{INIA\text{-}Pwinter} = 0.93$, $p < 0.0001$; $R^2_{INIA\text{-}Pannual}=0.89$, $p < 0.0001$) and temperature data ($R^2_{INIA\text{-}Twinter} = 0.83$, $p < 0.0001$; $R^2_{INIA\text{-}Tannual}=0.79$, $p < 0.0001$). The correlation analysis between meteorological parameters (i.e., annual and seasonal averaged temperature and precipitation) and sedimentological, geochemical proxies is shown in Table 4. In this, the varve thickness was retained as the main sedimentological proxy whereas the scores of the two first principal components PC1 and PC2 were chosen as geochemical proxies for grain-size (i.e., related to lake hydrodynamical conditions) and chemical weathering, respectively.

Among the selected proxies, the varve thickness was only sensitive to precipitation. The relationship between precipitation and varve was characterized by a Pearson correlation coefficient of −0.53 for annual precipitation and −0.71 in austral spring (i.e., September to November) (Table 4). As already presented in the first section of the discussion, such significant correlation supports the annually-resolved character of the sedimentation in LJe14B. The formation of clastic varves is mainly explained by seasonal runoff that carry suspended sediment into a stratified lake water body (Sturm, 1979). The thickness of the clastic varves, like the ones observed in core LJe14B, is strongly controlled by the amount of snowmelt-related runoff (e.g., Cockburn and Lamoureux, 2008). Such seasonally-contrasted sedimentation is reported worldwide in proglacial lakes (e.g., Leemann and Niessen, 1994, Gyuard et al., 2007). The coarse layer results of sediment settling during high hydrodynamic conditions whereas the fine silt and clay layers result of particle settling in the water column during calm conditions.

For Lake Jeinimeni record, the correlation with meteorological parameters (SM Fig. 7, Table 4) showed that the varve thickness in core LJe14B was controlled by the precipitation abundance and its related surface runoff. However, the observed correlation is negative meaning that thicker (thinner) varves characterize dry (wet) periods. This observation suggests some contribution of an aeolian transport in the LJe14B sedimentation. The steep and narrow topography of the Lake Jeinimeni valley favours windy conditions throughout the year. However, the wind control on sediment transport is probably more pronounced during the cold and locally dry austral summer corresponding to low runoff periods. A wind-control on varve thickness was proposed by Martin-Puertas et al. (2012) in the Meerfelder Maar record (Germany). In East Patagonia, the fastest winds that characterize the dry summer in the area may increase the erosive wave activity along the Lake Jeinimeni margins, providing detrital material to the lake. The fresh sedimentary deposits accumulated on the western margin of the Lake Jeinimeni during spring snowmelt could be especially sensitive to erosion and further transport by the lake hydrodynamic to the coring site.

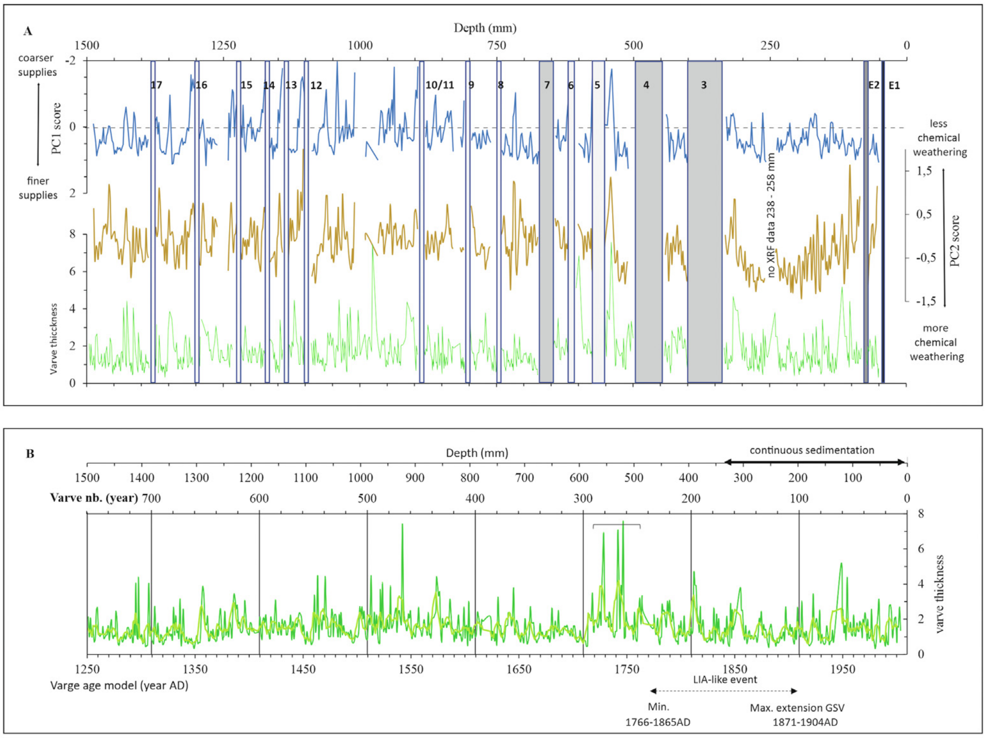

Fig. 6. A. Selected sedimentological and geochemical data of LJe14B reported *vs*. depth, i.e., PC1 and PC2 scores, and varve thickness in mm) The reported numbers correspond to the event layers observed in the core sedimentary features. B. Varve thickness is also reported *vs.* varve number (upper horizontal axis) and varve age model (lower horizontal axis) for comparison. The bold line represents a 5-years moving average curve. The horizontal bar underlines the interval characterized by the thickest varves. Its estimated age ca. 1750 CE is consistent with the oldest limit of the LIA-type event in North Patagonia, as reported by maximal and minimal extension of the Glacier San Rafael (GSR) in the Laguna San Rafael (Araneda et al., 2007). See text for more explanation.

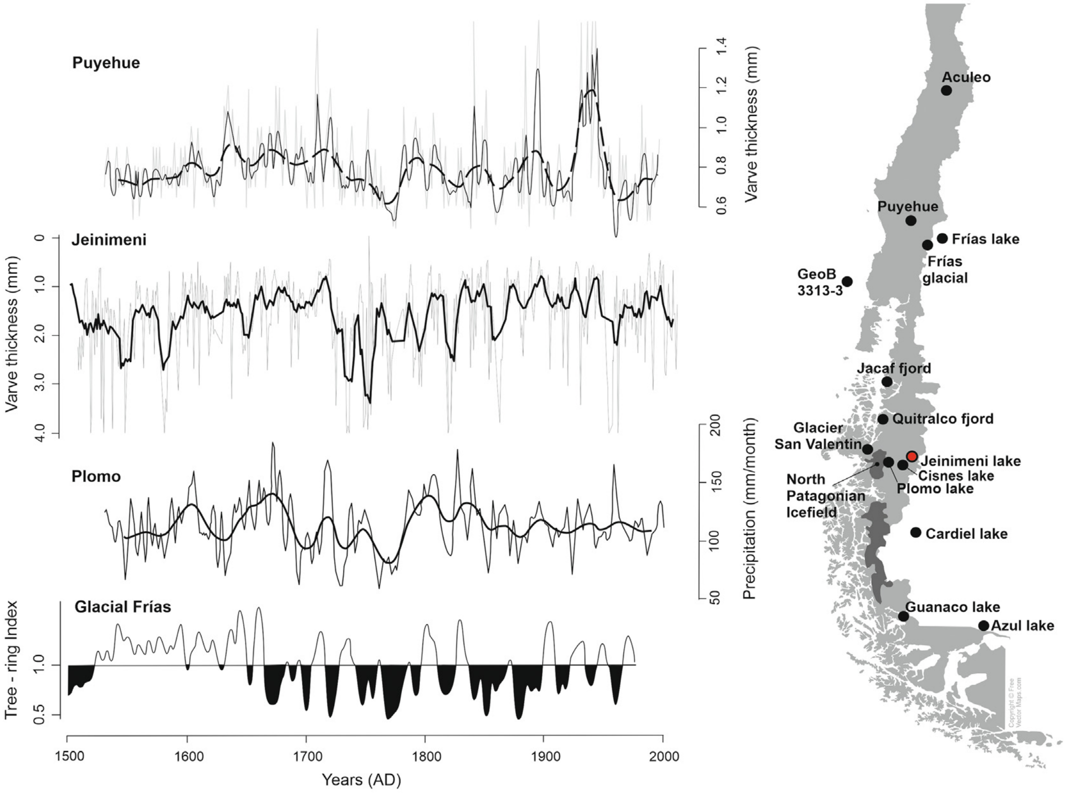

Fig. 7. Comparison of the varve thickness evolution of Lake Jeinimeni LJe14B with some regional records from lacustrine and glacial archives. (a) Varve thickness sequence back to 1530 CE obtained from the short core PUII of Lago Puyehue (40°S) by Boës and Fagel (2008). The varve thickness has been correlated to precipitation, the highest correlation being obtained for May, i.e. autumn/winter transition. The grey line represents the annual variations of the varve thickness, the dark grey line the 5-year filtered record and, the dashed black line the 30-year filtered. (b) Evolution of varve thickness of LJe14B for the last 500 years. The grey line represents the annual variations of the varve thickness, the black line the 10-year filtered record. (c) Reconstruction of austral winter (JJA) precipitation for varved sediments of Lago Plomo (46°59′S) derived from mass accumulation rate back to 1530 CE. The thin black line represents 5-year filtered precipitation data. The dashed line shows the 30 years filtered reconstruction. (d) Variations of tree-ring index on *Nothojagus pumilio* over the last 500 years (Villalba et al., 1990). The formation of wider tree-rings has been correlated to cold and rainy summers and to Glacial Frias re-advances. On the curve, the black arrows indicate the position of the Glacier Frias advances, their thickness being indicative of the event extension. Note all the curves indicate higher precipitation upwards. The location of the different records cited in the text is reported on the adjacent map on the right side of the figure. See text for more explanation.

Concerning the geochemical proxies, only PC1 presents a correlation with varve thickness, with thicker varves corresponding to higher PC1 scores ($R^2_{PC1\text{-}varve} = 0.54$, Table 4, SM Fig. 5). This correlation evidences an important contribution of sediment particle transport, and further settling, during calm hydrodynamic conditions expressed by positive PC1 score. Those conditions favour the transport of the finest clayey silt particles. This hypothesis would be confirmed by a counting of the individual thickness of the coarsest and the finest laminae that compose the clastic varves of Lake Jeinimeni sedimentary record. However, as said earlier in the laminae description, the core LJe14B does not allow to do such counting. Indeed, there is no clear distinction between the coarse grained and overlying fine-grained laminae but rather a gradual boundary.

In addition to varve thickness, the geochemical proxies were correlated to the first two principal components. PC1 score displays a negative correlation with austral winter temperature ($R^2_{JJA\text{-}PC1} = -0.54$, Table 4, SM Fig. 5). Lower austral winter temperatures favour snow accumulation and limits physical erosion. Only fine particulates (i.e., positive PC1) are transported to the lake, mostly by winter deflation. Again, the aeolian transport seems to contribute in a significant fraction of the particle settling in Lake Jeinimeni. The deployment of seasonal sediment traps within the water column would confirm this hypothesis.

On the contrary, PC2 score is positively correlated to temperature, but only with austral spring temperature ($R^2_{SON\text{-}PC2} = 0.58$, Table 4). For Lake Jeinimeni area, the austral spring warmer temperature is responsible for pronounced snow melting. The snowmelt delivers a high sedimentary load driven by La Gloria stream (reported on Fig. 1C) recorded by the high spring flow of the Jeinimeni River measured in Chile Chico station (Fig. 1B). The settling of such high sedimentary load explains the pluri-millimetre sandy-layers observed at the bottom part of the laminae couplet in LJe14B. In addition, the relationship between PC2 and SON temperature is marked by a lag of a few years (SM Fig. 5). An increase in the Sr and Ca content of the lake sediments (i.e., marked by a PC2 increase) occurs a few years later than a period of warmer SON temperatures. This observation suggests more influence of physical weathering than chemical one. Austral spring snowmelt upstream induces a downstream transport of less-chemically-weathered material to the coring site.

Another geochemical ratio, i.e. Si/Al, is also highly correlated with precipitation ($R^2_{annual\ P-Si/Al} = 0.72$), the highest correlation being observed in fall ($R^2_{MAM\text{-}Si/Al} = 0.75$). In the literature Si/Al has been used as a proxy for grain-size (Davies et al., 2015; Kylander et al., 2011). In core LJe14B, the correlation of Si/Al with austral winter temperature ($R^2_{JJA\text{-}Si/Al} = 0.50$) rather underlines a major runoff control. Indeed, the precipitation enhances physical weathering but also increase lake level. The overbank flooding reduces the energy hydrodynamics and favours the settling of fine particles .

5.4. *Environmental variability over the last millennium*

Various sedimentological, glacial and biological archives have been investigated in continental and also in marine settings from Southern America to reconstruct the climate variability over the last millennia. An overview of the regional information deduced from these different archives retrieved at different longitude is given for a 20° latitudinal transect from 33° to 53°S in South America (Table 5). Some studies depict a general overview of the changes over the Holocene whereas others present detailed reconstructions allowing to evidence short climate event like MCA or LIA-type events. In addition, historical archives may also provide information on pronounced environmental changes related to rapid climate events like the LIA. The temporal resolution of each archive is controlled by its accumulation rate or growth rate combined with the sampling step resolution.

Among the numerous archives, varve thickness is commonly used as a high-resolution proxy of climate change (e.g., Zolitschka, 1996; Kemp et al., 2001; Nederbragt and Thurow, 2001; Haberzettl et al., 2005). For Lake Jeinimeni setting, the meterological calibration evidences that varve thickness of core LJe14B mainly reflects precipitation intensity. Varve counting in LJe14B allows a reconstruction of precipitation over, at least, 759 ± 62 years, i.e., from ~1250 CE–2008. Note this time-window may be longer due to possible erosive influence of the events E3, 4 and 7 (Fig. 4C). The uncertainty on the age model precludes any time-series analysis. The sedimentary record of Lake Jeinimeni displays a pronounced multidecadal variability in varve thickness, by a factor of 1–8, over core depth (Fig. 6). This observation that claims for strong variability in local precipitation is consistent with Late Holocene climate variability observed in North Patagonia (e.g., Villalba et al., 1990; Markgraf et al., 2013, Sepulveda et al., 2009; Masiokas et al., 2009). The reconstructed annual precipitation curve in LJe14B (Fig. 7) evidences a succession of wet (ca. 1259–1350 CE, 1400–1450 CE, 1480–1490 CE, 1580–1610 CE, 1650–1690 CE, 1750–1800 CE, 1820–1850 CE, 1860–1920 CE and 1960–1990 CE) and dry (ca. 1380–1400 CE, 1700–1750 AD) intervals of variable, decadal to multidecadal, duration. Those climate fluctuations are roughly consistent to the Glacial Frias (41°09′S, 71°48′W - Fig. 7) fluctuations. Its dendrochonological-derived chronology is marked by 8 re-advances over the last 4 centuries at ca. 1638 CE, 1717–1727, 1742–1752, 1835–1843, 1875–1884, 1912–1916, 1942–1943, and 1977–1978 (reported in Fig. 7), each of those been characterized by a cold and rainy interval recorded by a wider tree ring (Villalba et al., 1990). In LJe14B, the most marked drier interval is characterized by a sharp drop of precipitation ca. 1700 CE and a more gradual return to wetter conditions at ca. 1750 CE. This dry interval precedes a wetter and colder phase reported from various North Patagonian archives such as tree rings (Villalba et al., 1990, 2003; Villalba, 1994; Luckman and Villalba, 2001), extensive glacier advances (Masiokas et al., 2009, 2010), marine (e.g., core GeoB3313-1, Fig. 7 - Lamy et al., 2001), fjord (Jacaf, Fig. 7 - Sepulveda et al., 2009) and lacustrine (Lago Plomo, Fig. 7 - Elbert et al., 2012) sediments between ca. 1780 CE and 1850) and attributed to the LIA-like

Table 5
Overview of regional paleoenvironmental information deduced from published climate archives reported over a 20° latitudinal transect from 33° to 53°S in South America.

Site	Lat. °S	Long. °W	Time slice kyr	Proxy	Observations	Ref.
Laguna Aculeo	33	70	2.0	Magn. susc.	Flood events marked by high clastic input at 200–400 CE, 500–700, 1300–1700 & 1850–1998 and recorded increased intensity of Westerlies (SWW).	1
Lago	40	72	0.6	Terrigenous supply	Wet phase 1500–1700 CE attributed to onset of LIA and strengthening of SWW north of 50°S.	2
Puyehue			0.6	Varve thickness	Increased varve thickness related to stronger SWW-related precipitation and higher lake level. Thin varves ca. 1400–1510 CE interpreted as warm MCA.	3
Laguna Frias	40	71	0.28	Varve thickness	A varved record ~ 1977–1713 CE displays increased varve thickness related to precipitation intensity and is roughly in agreement with Frias glacier advances. A cold and rainy period (LIA) is observed ca. 1873 CE.	4
Geo B3313-3	41	74.3	7.7	XRF Fe content	More humid conditions over the last 4 kyr, with less humid intervals around BC1450, over BC550-AD50 and BC50-AD350 and ~1200 CE. Increased rainfall related to an equatorward position of the SWW as during LIA whereas a decreased rainfall associated to a poleward shift is observed e.g., during MWP.	5
Jacaf Fjord	44	72.6	1.75	Biomarker Alkenone	Transition between a relatively dry/wet period before 1050 CE and wet/cold period after 1200 CE corresponding to MCA. The colder SST observed over 1200–1350 CE and 1500–1700 (LIA). The wetter/colder conditions reflect an equatorward position of the SSW.	6
Quitralco Fjord	45.7	72.5	1.4	Fe/Ti	Increased flood seasonality triggered by SWW precipitation over 600–1200 CE, reduced over 1200–1500 CE, lowest over 1500–1950 CE (LIA) and increased after 1950 CE. Interpreted in terms of latitudinal changes of the SWW over time with increased seasonality reflecting a poleward shift.	7
				Al/Ti Grain-size		
Lago Plomo	46.6	72.5	0.6	Varve thickness	Austral winter precipitation reconstruction showed 3 wetter phases ~ 1600 CE, 1600–1630 CE and 1780–1850 CE and a drier period ~ 1690–1780 CE. Pronounced decadal and multidecadal variability related to SWW.	8
Glacier San Valentin	41.3 −46.5	72.5 −75.3	>0.3	Reports maps	Major extension of Glacier San Valentin into the Laguna San Rafael over 1766–1890 CE, with the coldest period over 1857–1871 CE.	9
Lago Cisnes	47	72.2	6	δ18O in bivalve	Wetter conditions before 150 CE, followed by dried conditions with a minimum of evaporation at 1150 CE. Decreased SWW strength after 850 CE due to northwards SSW position and temperature drop.	10
Lago Cardiel	49	71	25	Paleo-shoreline	Lower lake level at 11.5–20, and 3.3–5.1 ka BP due to strong evaporation during stronger SWW. Northern migration of SWW observed over the last 5 ka.	11
Lago Guanaco	51.5	72.5	1.2	δ^{18}O ιν bivalve	Increased evaporation between 1150–1400 CE (MCA) and 1550–1900 CE (LIA). Poleward shift of the southern margin of SWW during LIA.	12
Lago Azul	52	69.3	11	Pollen, Ti, C/N	Intense SWW between ~10 and 8 kyr BP marked in East Patagonia by arid conditions (low lake level, low runoff, high littoral organic matter supplies). Intense SWW also observed over the last 3 ka	13
			11	Pollen	Periods of intensification of SWW correspond to a latitudinal contraction of the wind.	14
			1.0	δ^{13}Corg.	A marked lake level rise from 1670 CE to 1890 CE was induced by higher effective moisture during cooler and/or moister conditions (LIA)	15

References: 1. Jenny et al. (2002); 2. Bertrand et al. (2005); 3. Boës and Fagel, 2008; Aritzegui et al., 2007; 5. Lamy et al., 2001; 6. Sepulveda et al., 2009; 7. Bertrand et al., 2014; 8. Elbert et al., 2012; 9. Araneda et al., 2007; 10. Alvarez et al., 2015; 11. Quade and Kaplan (2017); 12. Moy et al., 2008; 13. Mayr et al., 2007; 14. Zolitschka et al., 2019; 15. Mayr et al. (2005).

interval. North Patagonian glacial fluctuations over the last 1000 years have been studied by Rabassa et al. (1979, 1984), Villalba et al. (1990) and Masiokas et al. (2010). Villalba et al. (1990) emphasized the major glacial advances of the Frias Glacier (Fig. 7) between 1800–1850 CE as the LIA event. Likely tree-ring dating indicated that the most extensive expansion of the Glacier Río Manso, (41°12′S, 71°51′W) over the past several centuries took place between the late 1700s and the 1830–40s as the glacier thickened and advanced into adjacent forests (Masiokas et al., 2009). Further south the LIA-like event has been identified by the evolution of the Glacier San Rafael (46°7′S 73°80′W - Fig. 7) located at similar latitude than Lake Jeinimeni but on the western side of the North Patagonian Icefield. Based on documentary archives, Araneda et al. (2007) reconstructed the minimal and maximal extension of the Glacier San Rafael within the adjacent laguna (see location on Fig. 1). They identified the interval comprised between 1766–1865 CE and 1871–1904 CE (Fig. 6) as an interval corresponding to the LIA-type event in North Patagonia. The coldest interval ca. 1857–1871 CE is consistent with literature compilation from Northern Patagonian Icefield (Masiokas et al., 2009). Indeed, the dating of moraines and trimlines associated with 12 North Patagonian glaciers outlets indicated major glacial advances between 1820–1850 CE (Masiokas et al., 2009), whereas the LIA is identified ≤100–300 yr earlier in South Patagonia (Koch and Kilian, 2005), e.g., between 1550–1800 CE (Moy et al., 2008). Therefore, the transition observed in LJe14B around 1750 CE is consistent with the oldest limit of the LIA-type event in North Patagonia, i.e. a youngest limit by comparison to the LIA interval for the Northern Hemisphere (i.e., 1570–1900 CE - Matthews and Briffa, 2005).

The regional significance of the climate variability of Lake Jeinimini record has been further assessed by the comparison with two varve sequences documented in North Chilean and Argentinean Patagonia (Fig. 7). In 2012, Elbert et al. (2012) reported an annually-laminated sedimentary record for 1530–2002 AD from a proglacial lake (Lago Plomo 46°59′S, 72°52′W, 203 masl - Fig. 7) located east of the Northern Patagonian Ice Field, at 75 km WSW of Lake Jeinimeni. Since no local meteorological station was available for the calibration, the mass accumulation rate (MAR) derived from the varves thickness were calibrated against austral winter (JJA) precipitation climate reconstruction data retrieved 47.0°S 72.5°W for the period 1930–2002 CE). By reference to the calibration period, the reconstructed winter precipitation curve (Fig. 7) evidenced 3 wetter intervals around 1600 CE, 1630–1690 CE and 1780–1850 CE, and a drier period 1690–1780 CE with a minimum at 1770 CE. Those intervals are roughly consistent with the wet and dry intervals identified in LJe14B (i.e., 1580–1610 CE, 1650–1690 CE, 1750–1800 CE and 1700–1750 CE). The time lag of 10–30 years remains within the calculated uncertainty of the varve counting in LJe14B (i.e., ±62 years).

Likely Aritzegui et al. (2007) investigated a 180 year-varve thickness record in a proglacial lake (Laguna Frias, Argentina, 40°S - Fig. 7). The authors emphasized that varve thickness variations mimict the Frias glacier (41°09′S, 71°48′W - Fig. 7) fluctuations (Villalba et al., 1990), with thicker varves during glacial readvances. Most of those glacier readvances have been recorded in Lago Frias by the sedimentation of a thicker detrital clayey to silty laminations, linked to the abrasion of the bedrock by the glacier.

Moreover, some regional-scale coherency with the LJe14B record is even observed with lacustrine sequences from Central Chile. A 600 year-varve sequence retrieved from Lago Puyehue (40°S, Fig. 7) was divided by 8 periods (Boës and Fagel, 2008; Fagel et al., 2008). The thin varve thickness from ca. 1400–1510 CE in Lake Puyehue is consistent with the dry period observed in LJe14B between 1400–1450 CE, had been interpreted as low lake level during the late MCA interval. The interval ca. 1510–1630 CE, characterized by thicker varves, indicated more humid conditions in central Chile in comparison with the present-day regional climate conditions. It covers two successive wet phases evidenced in LJe14B (i.e., 1480–1490 CE and 1580–1610) and was also recorded in Lake Plomo (ca. 1600 CE). Between ca. 1630 CE–1730 and 1780–1820 CE, two significant increases in varve thickness attested for another wetter phases, consistent with the wet LJe14B intervals at 1650–1690 CE and 1750–1800 CE but also with those recorded in the Lake Plomo record at 1630–1690 CE and 1780–1850 CE. There are interrupted by a drop in the precipitations from ca. 1730 CE–1780 that corresponds to dry intervals in LJe14B (~1700–1750 CE) and in Lake Plomo (~1690–1780 CE). The nineteen century mainly recorded wetter conditions in Lake Puyehue sequence, with a wet interval over 1820–1920 CE that covers 2 wet intervals evidenced in LJe14B at ca. 1820–1850 CE and 1860–1920 CE. The next wet interval evidenced in Lake Puyehue between 1920–1950 CE is not observed in LJe14B. Note the uppermost interval in the Lake Puyehue record was perturbed by an earthquake deposit at 1960 CE.

For a northern site, a multiproxy study of the sedimentary sequence of Laguna Aculeo (33°S, see location on Fig. 7) emphasized several clastic layers over the last 2 millennia (Jenny et al., 2002). Those deposits that occurred around ca. 200–400 CE, 500–700, 1300–1700 CE, and 1850–1998 CE were interpreted as floods and correlated with winter rains from the SWW (Jenny et al., 2002). The termination of the 1300–1700 CE flood event is consistent with the inception of the dry interval recorded between ca. 1700–1750 CE in LJe14B. The inception of the next flood event coincides with the end of the maximum extent of LIA as reported in North Patagonia (e.g., Araneda et al., 2007; Masiokas et al., 2009).

To summarize the regional overview, the precipitation record of Lake Jeinimeni is consistent with published paleoclimate reconstructions derived from different climate archives studied in Southern America.

6. Conclusion

The sedimentological and geochemical study carried out on Lake Jeinimeni sediments emphasizes environmental and climate variabilities in NE Chilean Patagonia, in agreement with climate reconstructions deduced from both marine and continental North Patagonian archives. The varved core LJe14B records recurrent hydrodynamical changes in the lake watershed, with seasonal clastic flood supplies related to austral spring temperature and snowmelt discharge. In addition, the presence of a few thick layers between 1700 and 1850AD underlines exceptional erosive conditions with the watershed responsible for major floods. The inverse relationship between varve thickness and precipitation indicates a contribution of aeolian transport within the LJe14b record during cold and dry austral summer. This could be especially true in lakes located in the forest-steppe ecotone like Lake Jeinimeni which is located in the lee side of the Patagonian Andes where an increase in the SWW could be reflected as an increase in aeolian transport of particles producing a thicker varve.

The climate interpretation is limited by the potential disturbance due to the deposition of those massive events. A distal coring site would bring a more continuous varved-record allowing to count individual laminae but also to perform spectral analyses on time-series and therefore further investigate the climate forcing. Precipitation-sensitive proxies (i.e., varve-thickness, Si/Al) display a high variability in the LJe14B sequence over at least 759 ± 62 years. The highest variability is reported for the oldest part of the LIA-type event (ca. 1750AD), in agreement with tree-ring records and glacial advances reported in North Patagonia, and quantitative precipitation reconstructions derived from lacustrine laminated sequences from both North Patagonia and Central Chile.

Author statement

N. Fagel was responsible for the redaction of the original draft, revised version and final editing of the manuscrit. She participed to the fieldrip, core description and sub-sampling. She interpreted the grain-size, mineralogical and geochemical data. She designed the Figs. 3 and 6, SM1, SM2 and tables SM1 and 2. She wrote the Belgian proposal for funding acquisition.P. Pedreros participed to the fieldrip and coring. He contributed to the meteorological data acquisition and was in charge of the statistical treatment and interpretation. He contributed to the Figs. 2 and 5, SM1, SM4 and Tables 2 and 3 He revised the last version of the manuscrit.D. Alvarez contributed to the bibliographic research and to the interpretation of the data. She was in charge of Figs. 4 and 7. She gave comments on both the original and revised texts.W. Tylmann did the varve counting and varve age model. He contribute to the redaction of the text on the core chronological section. He gave comments on the reviews.O. Namur gave his contribution for the preparation, analysis and interpretation of the tephra samples. He gave comments on the text and Fig. 3. A.C. Da Silva contributed to the data treatment, she gave comment on the original text and on the reviews.P. Jana contributed to the bibliographic research and data interpretation.A. Araneda led the fieldrip. He took part of the funding acquisition. He did the Fig. 1 and read the last version of the revised text before submission.I. Billy was in charge of the XRF and Scopix analyses. She revised the text of the methodological section.S. Schmidt was in charge for the preparation, analyses and interpretation of the Cs and Pb geochronometers. She contributed to the age model elaboration. She revised the methodological and chronological section of the manuscript.R. Urrutia took part to the Chilean funding acquisition. He gave his advise about the data interpretation.

Declaration of competing interest

The authors declare that they have no known competing financial interests or personal relationships that could have appeared to influence the work reported in this paper.

Acknowledgements

We thank Jorge Félez and Alex Henríquez from University of Concepcion for their help in elaboration of the geological and bathymetric maps; Isabel Israde Alcantara from the University of Morelia (Mexico) for diatom identification; Frederic Boulvain for thin section observation. This research was funded by WBI-Chile bilateral collaboration project and by Chilean Fondecyt funding 1201277. In addition, Roberto Urrutia thanks the project ANID/FONDAP/15130015 and Pablo Pedreros the Fondecyt Postdoctoral funding 3180356.

Appendix A. Supplementary data

Supplementary data to this article can be found online at https://doi.org/10.1016/j.quascirev.2021.107134.

References

Abbott, M.B., Stafford, T.W., 1996. Radiocarbon geochemistry of modern and ancient arctic lake systems, Baffin Island, Canada. Quat. Res. 45, 300–311.

Albéric, P., Jézéquel, D., Bergonzini, L., Chapron, E., Viollier, E., Massault, M., Michard, G., 2016. Carbon cycling and organic radiocarbon reservoir effect in a Meromictic crater lake (lac Pavin, Puy-de-Dôme, France). Radiocarbon 55, 1029–1042.

Alvarez, D., Fagel, N., Araneda, A., Jana-Pinninghoff, P., Keppens, E., Urrutia, R., 2015. Late Holocene climate variability on the eastern flank of the Patagonian Andes (Chile): a δ18O record from mollusks in Lago Cisnes (47°S). 25(8). Search Google Scholar for this author Holocene vol. 25, 1220–1230.

Appleby, P.G., Oldfield, F., 1978. The calculation of lead-210 dates assuming a constant rate of supply of unsupported 210Pb to the sediment. Catena 5, 1–8.

Aritzegui, D., Bösch, P., Davaud, E., 2007. Dominant ENSO frequencies during the Little ice age in northern Patagonia: the varved record of proglacial Lago Frías, Argentina. Quat. Int. 161, 46–55.

Araneda, A., Torrejón, F., Aguayo, M., Torres, L., Crucres, F., Cisternas, M., Urrutia, R., 2007. Historical records of san Rafael glacier adavances (North Patagonia icefield): another clue to 'Little ice age' in southern Chile? Holocene 17 (7), 989–1000.

Avşar, U., Hubert-Ferrari, A., De Batist, M., Fagel, N., 2014. A 3400 years lacustrine paleoseismic record from the North Anatolian Fault, Turkey: implications for bimodal recurrence behaviour. Geophys. Res. Lett. 41, 3773–3784. https://doi.org/10.1002/2013GL058221.

Bertrand, S., Boës, X., Castiaux, J., Charlet, F., Urrutia, R., Espinoza, C., Lepoint, G., Charlier, B., Fagel, N., 2005. Temporal evolution of sediment supply in Lago Puyehue (Southern Chile) during the last 600 yr and its climatic significance. Quat. Res. 64, 163–175.

Bertrand, S., Araneda, A., Vargas, P., Jana, P., Fagel, N., Urrutia, R., 2012. Using the N/C ratio to correct bulk radiocarbon ages from lake sediments: insights from Chilean Patagonia. Quat. Geochronol. 12, 23–29. https://doi.org/10.1016/j.quageo.2012.06.003.

Bertrand, S., Hughen, K., Sepúlveda, J., Pantoja, S., 2014. Late Holocene covariability of the southern westerlies and sea surface temperature in northern Chilean PatagoniaQuaternary. Sci. Rev. (Manila) 105, 195–208.

Blaauw, M., 2010a. Methods and code for 'classical' age-modelling of radiocarbon sequences. Quat. Geochronol. 5 (5), 512–518. https://doi.org/10.1016/j.quageo.2010.01.002.

Blaauw, M., 2010b. R-Code for 'classical' age-modelling (CLAM V1.0) of radiocarbon sequences. PANGAEA. https://doi.org/10.1594/PANGAEA.873023.

Boës, X., Fagel, N., 2008. Relationships between southern Chilean varved lake sediments, precipitation and ENSO for the last 600 years. J. Paleolimnol. 39, 237–252. https://doi.org/10.1007/s10933-007-9119-9.

Boës, X., Rydberg, J., Martinez-Cortizas, A., Bindler, R., Renberg, I., 2011. Evaluation of conservative lithogenic elements (Ti, Zr, Al, and Rb) to study anthropogenic element enrichments in lake sediments. J. Paleolimnol. 46, 75–87.

Boski, T., Pessoa, J., Pedro, P., Thorez, J., Dias, J.M.A., Hall, I.R., 1998. Factors governing abundance of hydrolysable amino acids in the sediments from the N.W. European Continental Margin (47–50°N). Prog. Oceanogr. 42, 145–164.

Bradley, R.S., Briffa, K.R., Cole, J., Hughes, M.K., Osborn, T.J., 2003. The climate of the last millennium. In: Alverson, K.D., Bradley, R.S., Pederson, T.F. (Eds.), Paleoclimate, Global Change and the Future. Springer, New York, pp. 105–141.

Chapron, E., Ariztegui, D., Mulsow, S., Villarosa, G., Pino, M., Outes, V., Juvigné, E., Crivelli, E., 2006. Impact of the 1960 major subduction earthquake in Northern Patagonia. Quat. Int. 158, 58–71.

Cherniak, D.J., 2002. Ba diffusion in feldspars. Geochem. Cosmochim. Acta 66 (9), 1641–1650.

Cockburn, J.M.H., Lamoureux, S.F., 2008. Inflow and lake controls on short-term mass accumulation and sedimentary particle size in a High Arctic lake: implications for interpreting varved lacustrine sedimentary records. J. Paleolimnol. 40 (3), 923–942. https://doi.org/10.1007/s10933-008-9207-5.

Corporación Nacional Forestal CONAF, 2017. Plan de uso público Reserva Nacional Lago Jeinimeni. República de Chile-Ministerio de Agricultura, pp. 27–30.

Cook, H.E., Johnson, P.D., Matti, J.C., Zemmels, I., 1975. Methods of sample preparation and X-ray diffraction data analysis in: X-ray mineralogy laboratory. In: Kaneps, A.G. (Ed.), Initial Reports of the DSDP. Printing Office, Washington, DC, pp. 997–1007.

Davies, S.J., Lamb, H.F., Roberts, S.J., 2015. Micro-XRF Core scanning in paleolimnology: recent developments. In: Croudarce, I.W., Rothwell, R.G. (Eds.), Micro-XRF Studies of Sediment Cores. Developments in Paleoenvironmental Research 17. Springer Science, Dordrecht, pp. 189–226.

Davis, J.C., 2002. Statistics and Data Analysis in Geology. J. Wiley & sons, New York, p. 638.

De la Cruz, R., Suarez, M., Formato, M., 2003. Geologia del area puerto guadal-puerto sanchez, region aisen del general carlos ibanez del campo, escala 1. 100000. n° mapa: m113. Servicio Nacional de Geologia y Mineria-Chile, Santiago.

Dirección General de Aeronáutica Civil DGAC, 2020. Anuario Meteorológico 2019. Editorial Dirección Meteorológica de Chile, Santiago de Chile. DGAC, pp. 85–86. https://climatologia.meteochile.gob.cl/application/index/anuarios.

Elbert, J., Grosjean, M., von Gunten, L., Urrutia, R., Fischer, D., Wartenburger, R., Ariztegui, D., Fujak, M., Hamann, Y., 2012. Quantitative high-resolution winter (JJA) precipitation reconstruction from varved sediments of Lago Plomo 47°S, Patagonian Andes, AD 1530-2002. Holocene 22 (4), 465–474. https://doi.org/10.1177/0959683611425547.

Encinas, A., Folguera, A., Riffo, R., Molina, P., Fernandez Paz, L., Litvak, V.D., Colwyn, D.A., Valencia, V.A., Carrasco, M., 2018. Cenozoic basin evolution of the Central Patagonian Andes: evidence from geochronology, stratigraphy, and geochemistry. Geosci. Front. https://doi.org/10.1016/j.gsf.2018.07.004.

Escobar, F., Vidal, F., Garin, C., Naruse, R., 1992. Water balance in the Patagonian icefield. In: Naruse, R., Aniya, M. (Eds.), Glaciological Researches in Patagonia, 1990. Japanese Society of Snow and Ice, pp. 109–119.

Fagel, N., Boës, X., Loutre, M.F., 2008. Climate oscillations evidenced by spectral analysis of Southern Chilean lacustrine sediments: the assessment of ENSO over the last 600 years. J. Paleolimnol. 39, 253–266.

Fagel, N., Alvarez, D., Namur, O., Devidal, J.L., Nuttin, L., Schmidt, S., Jana, P., Torrejon, F., Bertrand, S., Araneda, A., Urrutia, R., 2017. Lacustrine record of last millenia eruptions in Northern Chilean Patagonia (45-47°S). Holocene. https://doi.org/10.1177/0959683616687380.

Folk, R.L., Ward, W.C., 1957. A study in the significance of grain-size parameters. J. Sediment. Petrol. 27, 3–26.

Fuenzalida, R., 1976. The Hudson volcano. In: Proceedings of the IAVCEI Symposium on Andean and Antarctic Volcanology Problems, vols. 78–87. Santiago, Chile, 1974.

Garreaud, R.D., 2007. Precipitation and circulation covariability in the extratropics. J. Clim. 20, 4789–4797. https://doi.org/10.1175/JCLI4257.1.

Garreaud, R.D., Vuille, M., Compagnucci, R., Marengo, J., 2009. Present-day south America climate. Paleogeogr. Paleoclimatol. Palaeoecol. 281, 180–195.

Garreaud, R.D., Lopez, P., Minvielle, M., Rojas, M., 2013. Large-scale control on the Patagonian climate. J. Clim. 26, 215–230. https://doi.org/10.1175/JCLI-D-12-00001.1.

Gilli, A., Ariztegui, D., Anselmetti, F.S., McKenzie, J., Markgraf, V., Hajdas, I., McCulloch, R.D., 2005. Mid-Holocene strengthening of the southern westerlies in South America–sedimentological evidences from Lago Cardiel, Argentina (49°S). Global Planet. Change 49, 75–93.

Glasser, N.F., Jansson, K.N., Harrison, S., Kleman, J., 2008. The glacial geomorphology and Pleistocene history of South America between 38° and 56°S. Quat. Sci. Rev. 27, 365–390.

Glasser, N.F., Harrison, S., Schnabel, C., Fabel, D., Jansson, K.N., 2012. Younger Dryas and early Holocene age glacier advances in Patagonia. Quat. Sci. Rev. 58, 7–17.

Gyuard, H., Chapron, E., St-Onge, G., Anselmetti, F.S., Arnaud, F., Magand, O., Francus, P., Mélières, M.A., 2007. High-altitude varve records of abrupt environmental changes and mining activity over the last 4000 years in the Western French Alps (Lake Bramant, Grandes Rousses Massif). Quat. Sci. Rev. 26, 2644–2660.

Haberzettl, T., Fey, M., Lücke, A., Maidana, N., Mayr, C., Ohlendorf, C., Schäbitz, F., Schleser, G.H., Wille, M., Zolitschka, B., 2005. Climatically induced lake level changes during the last two millennia as reflected in sediments of Laguna Potrok Aike, southern Patagonia Patagonia (Santa Cruz, Argentina). J. Paleolimnol. 33, 283–302.

Harris, I.C., Jones, P.D., 2020. CRU TS4.03: Climatic Research Unit (CRU) Time-Series (TS) Version 4.03 of High-Resolution Gridded Data of Month-By-Month Variation in Climate (Jan. 1901- Dec. 2018). Centre for Environmental Data Analysis. https://doi.org/10.5285/10d3e3640f004c578403419aac167d82, 10.5285/10d3e3640f004c578403419aac167d82. (Accessed 22 January 2020).

Hepp, C., Reyes, C., Muñoz, R., 2018. Análisis de datos históricos de cinco estaciones meteorológicas de la región de Aysén. Boletín Técnico N°365. Instituto de Investigaciones Agropecuarias, Centro de Investigación INIA Tamel Aike, Coyhaique, Aysén-Patagonia, Chile, p. 200 (In Spanish).

Hedges, J.I., Stern, J.H., 1984. Carbon and nitrogen determinations of carbonate-containing solids. Limnol. Oceanogr. 29 (3), 657–663, 1984.

Henríquez, M., Alvear, N., 1987. Guía de Manejo Reserva Nacional Lago Jeinimeni. República de Chile-Ministerio de Agricultura, Corporación Nacional Forestal (CONAF), p. 42 (In Spanish).

Hein, A.S., Hulton, N.R.J., Dunai, T.J., Schnabel, C., Kaplan, M.R., Naylor, M., Xu, S., 2009. Middle Pleistocene glaciation in Patagonia dated by cosmogenic-nuclide measurements on outwash gravels. Earth Planet Sci. Lett. 286 (1–2), 184–197.

Hein, A.S., Hulton, N.R.J., Dunai, T.J., Sugden, D.E., Kaplan, M.R., Xu, S., 2010. The chronology of the Last Glacial Maximum and deglacial events in central Argentine Patagonia. Quat. Sci. Rev. 29, 1212–1227.

Heiri, A., Lotter, F., Lemcke, G., 2001. Loss on ignition as a method for estimating organic and carbonate content in sediments: reproducibility and comparability of results. J. Paleolimnol. 25 (1), 101–110.

Heusser, L., Heusser, C., Pisias, N., 2006. Vegetation and climate dynamics of southern Chile during the past 50,000 years: results of ODP Site 1233 pollen analysis. Quat. Sci. Rev. 25, 474–485.

Hogg, A.G., Hua, Q., Blackwell, P.G., Niu, M., Buck, C.E., Guilderson, T.P., Heaton, T.J., Palmer, J.G., Reimer, P.J., Reimer, R.W., Turney, C.S.M., Zimmerman, S.R.H., 2013. SHCal13 southern Hemisphere calibration, 0–50,000 Years cal BP. Radiocarbon 55 (4), 1889–1903.

Jenny, B., Valero-Garces, B.L., Urrutia, R., Kelts, K., Veit, H., Appleby, P.G., Geyh, M., 2002. Moisture changes and fluctuations of the westerlies in Mediterranean Central Chile during the last 2000 years: the laguna Aculeo record (33’50°S). Quat. Int. 87, 3–18.

Kemp, A.E.S., Dean, J., Pearce, R.B., Pike, J., 2001. Recognition and analysis of bedding and sediment fabric features. In: Last, Smol (Ed.), Tracking Environmental Change Using Lake Sediments. Physical and Geochemical Methods, vol. 2. Kluwer Academic Publishers, Dordrecht, The Netherlands, pp. 7–22.

Kylander, M., Ampel, L., Wohlfarth, B., Veres, D., 2011. High-resolution X-ray fluorescence core scanning analysis of Les Echets (France) sedimentary sequence: new insights from chemical proxies. J. Quat. Sci. 26, 109–117.

Koch, J., Kilian, R., 2005. “Little ice age” glacier fluctuations, Gran Campo Nevado, southernmost Chile. Holocene 15, 20–28.

Lamy, F., Hebbelm, D., Rohl, U., Wefer, G., 2001. Holocene rainfall variability in southern Chile: a marine record of latitudinal shifts of the southern westerlies. Earth Planet Sci. Lett. 185, 369–382.

Lamy, F., Kilian, R., Arz, H.W., Francois, J.P., Kaiser, J., Prange, M., Steinke, T., 2010. Holocene changes in the position and intensity of the southern westerly wind belt. Nat. Geosci. 3, 695–699.

Leemann, A., Niessen, F., 1994. Varve formation and the climatic record in an Alpine proglacial lake: calibrating annually laminated sediments against hydrological and meteorological data. Holocene 4, 1–8.

Luckman, B.H., Villalba, R., 2001. Assessing the synchroneity of glacier fluctuations in the western cordillera of the Americas during the last millennium. In: Markgraf, V. (Ed.), Interhemispheric Climate Linkages. Academic Press, New York, pp. 119–137.

Luebert, F., Pliscoff, P., 2006. Sinopsis bioclimática y vegetacional de Chile. Editorial Universitaria, Santiago.

Mann, M.E., Zhang, Z.H., Rutherford, S., Bradley, R.S., Hughes, M.K., Shindell, D., Ammann, C., Faluvegi, G., Ni, F.B., 2009. Global signatures and dynamical origins of the Little Ice Age and Medieval climate anomaly. Science 326, 1256–1260.

Markgraf, V., 1993. Paleoenvironments and paleoclimates in Tierra del Fuego and southernmost Patagonia, South America. Palaeogeogr. Palaeoclimatol. Palaeoecol. 102 (1–2), 53–68.

Markgraf, V., Dodson, J.R., Kershaw, A.P., McGlone, M.S., Nicholls, N., 1992. Evolution of late Pleistocene and Holocene climates in the circum-south Pacific land areas. Clim. Dynam. 6, 193–211.

Markgraf, V., Bradbury, J.P., Schwalb, A., Burns, S.J., Stern, C., Ariztegui, D., Gilli, A., Anselmetti, F.S., Stine, S., Maidana, N., 2003. Holocene palaeoclimates of southern Patagonia: limnological and environmental history of Lago Cardiel, Argentina (49°S). Holocene 13 (4), 581–591.

Markgraf, V., Whitlock, C., Haberle, S., 2007. Vegetation and fire history during the last 18,000 cal yr B.P. in Southern Patagonia: Mallín Pollux, Coyhaique, Province Aisén (45°41′30″ S, 71°50′30″ W, 640 m elevation). Palaeogeogr. Palaeoclimatol. Palaeoecol. 254, 492–507.

Markgraf, V., Iglesias, V., Whitlock, C., 2013. Late and postglacial vegetation and fire history from Cordón Serrucho Norte, northern Patagonia. Palaeogeogr. Palaeoclimatol. Palaeoecol. 371, 109–118.

Martin-Puertas, C., Brauer, A., Dulski, P., 2012. Testing climate–proxy stationarity throughout the Holocene: an example from the varved sediments of Lake Meerfelder Maar (Germany). Quat. Sci. Rev. 58, 56–65.

Masiokas, M.H., Luckman, B.H., Villalba, R., Delgado, S., Skvarca, P., Ripalta, A., 2009. Little Ice Age fluctuations of small glaciers in the Monte Fitz Roy and Lago del Desierto areas, south Patagonian Andes, Argentina. Palaeogeogr. Palaeoclimatol. Palaeoecol. 281, 351–362.

Masiokas, M.H., Luckman, B.H., Villalba, R., Ripalta, A., Rabassa, J., 2010. Little ice age fluctuations of glaciar Río Manso in the North Patagonian Andes of Argentina. Quat. Res. 73, 96–106.

Masson-Delmotte, V., et al., 2013. In climate change. In: Stocker, T.F., et al. (Eds.), The Physical Science BasisContribution of Working Group I to the Fifth Assessment Report of the Intergovernmental Panel on Climate Change. Cambridge Univ. Press, pp. 383–464.

Matthews, J.A., Briffa, K.R., 2005. The ‘Little ice age’: Re-evaluation of an evolving concept. Geogr. Ann. 87, 17–36.

Mayr, C., Lücke, A., Wagner, S., Wissel, H., Ohlendorf, C., Haberzettl, T., Oehlerich, M., Schäbitz, F., Wille, M., Zhu, J., 2013. Intensified Southern Hemisphere Westerlies regulated atmospheric CO2 during the last deglaciation. Geology 41, 831–834.

Mayr, C., Fey, M., Haberzettl, T., et al., 2005. Palaeoenvironmental changes in southern Patagonia during the last millennium recorded in lake sediments from Laguna Azul (Argentina). Palaeogeogr. Palaeoclimatol. Palaeoecol. 228, 203–227.

Mayr, C., Wille, M., Haberzettl, T., et al., 2007. Holocene variabilityof the southern Hemisphere westerlies in argentinean Patagonia (52°S). Quat. Sci. Rev. 26, 579–584.

Meyers, P.A., Teranes, J.L., 2001. Sediment organic matter. In: Last, W.M., Smol, J.P. (Eds.), Tracking Environmental Change Using Lake Sediments, Vol. Volume 2, Physical and Geochemical Methods. Kluwer Academic Publishers, Dordrecht, Netherlands, pp. 239–269.

Moernauts, J., Van Daele, M., Fontijn, K., Kempf, P., Pino, M., Valdebenito, G., Urrutia, R., Strasser, M., De Batist, M., 2018. Larger earthquakes recur more periodically: new insights in the megathrust earthquakes cycle in lacustrine turbidite records in south-central Chile. Earth Planet Sci. Lett. 481, 9–19.

Montecinos, A., Aceituno, P., 2003. Seasonality of the ENSO-related rainfall variability in Central Chile and associated circulation anomalies. Am. Meteorol. Soc. 16, 281–296.

Moore, D., Reynolds Jr., R.C., 1997. X-Ray Diffraction and the Identification and Analysis of Clay Minerals. Oxford University Press, Oxford, p. 332.

Moreno, P.I., Jacobson, G.L., Lowell, T.V., Denton, G.H., 2001. Interhemispheric climate links revealed by a late-glacial cooling episode in southern Chile. Nature 409, 804–808. https://doi.org/10.1038/35057252.

Moreno, P.I., Francois, J.P., Villa-Martinez, R.P., Moy, C.M., 2009. Millennial-scale variability in Southern Hemisphere westerly wind activity over the last 5000 years in SW Patagonia. Quat. Sci. Rev. 28, 25–38. https://doi.org/10.1016/j.quascirev.2008.10.009.

Moy, C.M., Dunbar, R.B., Moreno, P.I., Francois, J.P., Villa-Martínez, R., Mucciarone, D.M., Guilderson, T.P., Garreaud, R.D., 2008. Evidence for hydrologic change related to the westerlies in SW Patagonia, Chile, during the last millennium. Quat. Sci. Rev. 27, 1335–1349. https://doi.org/10.1016/j.quascirev.2008.03.006.

Moy, C.M., Moreno, P.I., Dunbar, R.B., Kaplan, M.R., Francois, J.P., Villalba, R., Haberzettl, T., 2009. Climate change in Southern South America during the last 2 millennia. In: Vimeux, et al. (Eds.), Past Climate Variability in South America and Surrounding Regions. Developments in Paleoenvironmental Research, vol. 14, pp. 353–387. https://doi.org/10.1007/978-90-481-2672-9_15.

Moy, C.M., Dunbar, R.B., Guilderson, T.P., Waldmann, N., Mucciarone, D.A., Recasens, C., Ariztegui, D., Austin Jr., J.A., Anselmetti, F.S., 2011. A geochemical and sedimentary record of high southern latitude Holocene climate evolution from Lago Fagnano, Tierra del Fuego. Earth Planet Sci. Lett. 302, 1–13.

Mulder, T., Syvitski, J.P.W., Skene, K.I., 1998. Modelling of erosion and deposition by turbidity currents generated at river mouths. J. Sediment. Res. 68, 124–137.

Naranjo, J.A., Stern, C.R., 1998. Holocene explosive activity of Hudson volcano, southern Andes. Bull. Volcanol. 59, 291–306.

Naranjo, J.A., Moreno, H., Banks, N.G., 1993. La erupción del volcán Hudson en 1991 (46°S), Región de Aisén, Chile. Servicio Nacional de Geología y Minería, Boletin 44 Santiago, p. 50.

Naranjo, J.A., Stern, C.R., 2004. Holocene tephrochronology ofthe southernmost part (42°–45°S) of Andean Southern Volcanic Zone. Revista Geológica de Chile 31, 225–240.

National Center for Atmospheric Research Staff, 2017. The Climate Data Guide CRU TS Gridded Precipitation and Other Meteorological Variables since 1900. NCAR. Retrieved from. https://climatedataguide.ucar.edu/climate-data/cru-ts-gridded-precipitation-and-other-meteorological-variables-1901.

Nederbragt, A.J., Thurow, J.W., 2001. A 6000 years varve record of Holocene climate in Saanich Inlet, British Columbia, from digital sediment colour analysis of ODP Leg 169S cores. Mar. Geol. 174, 95–110.

Neukom, R., Luterbacher, J., Villalba, R., Kuttel, M., Frank, D., Jones, P.D., Grosjean, M., Esper, J., Lopez, L., Wanner, H., 2010. Multi-centennial summer and winter precipitation variability in southern South America. Geophys. Res. Lett. 37.

Neukom, R., Steiger, N., Gómez-Navarro, J.J., et al., 2019. No evidence for globally coherent warm and cold periods over the preindustrial Common Era. Nature 571, 550–554. https://doi.org/10.1038/s41586-019-1401-2.

New, M., Lister, D., Hulme, M., Makin, I., 2002. A high-resolution data set of surface climate over global land areas. Clim. Res. 21, 1–25. https://doi.org/10.3354/cr021001.

Orihashi, Y., Naranjo, J.A., Motoki, A., Sumino, H., Hirata, D., Anma, R., Nagao, K., 2004. Quaternary volcanic activity of Hudson and Lautaro volcanoes, Chilean Patagonia: new constraints from K-Ar ages. Rev. Geol. Chile 31 (2), 207–224. https://doi.org/10.4067/S0716-02082004000200002.

Pankhurst, R.J., Weaver, S.D., Hervé, F., Larrondo, P., 1999. Mesozoic-cenozoic evolution of the north Patagonian batholith in aysen, southern Chile. J. Geol. Soc. 156 (4), 673–694.

Pfeiffer, M., Mascayano, C., Aburto, F., 2010. Soils of Chilean Patagonia in glacial and periglacial environments. Eurasian Soil Sci. 43 (13), 1430–1438.

Quade, J., Kaplan, M.R., 2017. Lake-level stratigraphy and geochronology revisited at Lago (lake) Cardiel, Argentina, and changes in the southern Hemispheric westerlies over the last 25 ka. Quat. Sci. Rev. 177, 173–188.

Quiroz, R., Popp, P., Urrutia, R., Bauer, C., Araneda, A., Treutler, H.C., Barra, R., 2005. PAH fluxes in the Laja Lake of south central Chile Andes over the last 50 years: evidence from a dated sediment core. Sci. Total Environ. 349, 150–160.

Rabassa, J., Rubulis, S., Suarez, J., 1979. Rate of formation and sedimentology of (1976–1978) push-moraines, Frıas glacier, mount Tronador (41°10S, 71°53W), Argentina. In: Schlüchter, Ch (Ed.), Moraines and Varves, pp. 65–79. Rotterdam, Balkema.

Rabassa, J., Brandani, A., Boninsegna, J.A., Cobos, D.R., 1984. Cronología de la “PequeñaEdad del Hielo” en los glaciares Río Manso y Castaño Overo, Cerro Tronador, Provincia de Río Negro, 3, 624–639. Noveno Congreso Geológico Argentino, Actas.

R Development Core Team, 2016. R: A Language and Environment for Statistical Computing. R Foundation for Statistical Computing, Vienna, Austria, 3-900051-07-0, URL. http://www.R-project.org/.

Revelle, W., 2017. Psych: Procedures for Personality and Psychological Research. North- Western University. Evanston. R package version 1.7.12. URL. http://personality-project.org/r/psych.

Richter, T.O., Van der Gaast, S., Koster, B., Vaars, A., Gieles, R., De Stigter, H., De Haas, H., van Weering, T.C.E., 2006. The Avaatech XRF core scanner: technical description and applications to NE Atlantic sediments. In: Rothwell, R.G. (Ed.), New Techniques in Sediment Core Analysis. Special Publication, vol. 267. Geological Society, London, pp. 39–50.

Rothwell, R.G., Rack, F.R., 2006. New techniques in sediment core analysis: an introduction. In: Rothwell, R.G. (Ed.), New Techniques in Sediment Core Analysis. Special Publication, vol. 267. Geological Society, London, pp. 1–29.

Rothwell, R.G., Croudace, I.W., 2015. Twenty years of XRF core scanning marine sediments: what do geochemical proxies tell us? In: Croudarce, I.W., Rothwell, R.G. (Eds.), Micro-XRF Studies of Sediment Cores. Developments in Paleoenvironmental Research 17. Springer Science, Dordrecht, pp. 189–226. https://doi.org/10.1007/978-94-017-9849-5-7.

Scasso, R.A., Carey, S., 2005. Morphology and fotmation ofglassy volcanic ash from the august 12-15, 1991 eruption of Hudson volcano, Chile. Lat. Am. J. Sedimentol. Basin Anal. 12 (1), 3–21.

Schimpf, D., Kilian, R., Kronz, A., Simon, K., Spotl, C., Worner, G., Deininger, M., Mangini, A., 2011. The significance of chemical, isotopic, and detrital components in three coeval stalagmites from the superhumid southernmost Andes (53S) as high-resolution palaeo-climate proxies. Quat. Sci. Rev. 30, 443–459.

Sepulveda, J., Pantoja, S., Hughen, K.A., Bertrand, S., Figueroa, D., León, T., Drenzek, N.J., Lange, C., 2009. Late Holocene sea-surface temperature and precipitation variability in northern Patagonia, Chile (Jacaf Fjord, 44°S). Quat. Res. 72, 400–409.

Siegenthaler, C., Sturm, M., 1991. Slump induced surges and sediment transport in Lake Uri, Switzerland. Int. Assoc. Theor. Appl. Limnol. Proc. 24 (2), 955–958.

Sperazza, M., Moore, J., Hendrix, M., 2004. High-resolution particle size analysis of naturally occurring very fine-grained sediment through laser diffractometry. J. Sediment. Res. 74 (5), 736–743.

Stern, C.R., 2004. Active andean volcanism: its geologic and tectonic setting. Rev. Geol. Chile 31 (2), 161–206.

Stern, C.R., de Porras, M.E., Maldonado, A., 2015. Tephrochronology of the upper Río Cisnes valley (44°S), southern Chile. Andean Geol. 42 (2), 173–189.

Stupar, Y.V., Schäfer, J., García, M.G., Schmidt, S., Piovano, E., Blanc, F., Huneau, G., Le Coustumer, P., 2014. Historical mercury trends recorded in sediments from the Laguna del Plata, Córdoba, Argentina. Chemie der Erde Geochim. 74, 353–363.

Sturm, M., 1979. Origin and composition of clastic varves. In: Schlüchter, C. (Ed.), Moraines and Varves: Origin, Genesis, Classi**fi**cation. A.A. Balkema, Rotterdam, The Netherlands, pp. 281–285. http://www.worldcat.org/title/moraines-andvarves-origin-genesis-classification/oclc/5542145.

Thomson, S.N., 2002. Late Cenozoic geomorphic and tectonic evolution of the Patagonian Andes between latitudes 42°S and 46°S: an appraisal based on fission-track results from the transpressional intra-arc Liquiñe-Ofqui fault zone. Geol. Soc. Am. Bull. 114 (9), 1159–1173.

Trenbeth, K.E., 1991. Storm tracks in the southern Hemisphere. J. Atmos. Sci. 48 (19), 2159–2178.

Turner, K.J., Fogwill, C.J., McCulloch, R.D., Sugden, D.E., 2005. Deglaciation of the eastern flank of the North patagonian icefield and associated continentaol-scale lake diversions. Geografiska Annaler 87A (2), 363–374.

Unkel, I., Fernandez, M., Bjorck, S., Ljung, K., Wohlfarth, B., 2010. Records of environmental changes during the Holocene from Isla de los Estados (54.4°S), southeastern Tierra del Fuego. Global Planet. Change 74, 99–113.

Vandekerkhove, E., Bertrand, S., Reid, B., Bartels, A., Charlier, B., 2015. Sources of dissolved silica to the fjords of northern Patagonia (44-48°S): the importance of volcanic ash soil distribution and weathering Earth. Surf. Process. Landforms. https://doi.org/10.1002/esp.3840.

Vanneste, K., Wils, K., Van Daele, M., 2018. Probabilistic evaluation of fault sources based on paleoseismic evidence from mass-transport deposits: the example of Aysén Fjord, Chile. J. Geophys. Res.: Solid Earth 123, 9842–9865. https://doi.org/10.1029/2018JB016289.

Villalba, R., 1994. Tree-ring and glacial evidence for the Medieval warm epoch and the Little ice age in southern South America. Climate Change 26, 183–197.

Villalba, R., Leiva, J.C., Rubulis, S., Suarez, J., Lenzano, L., 1990. Climate tree-rings and glacial fluctuations in the Rio Frias valley, Rio Negro, Argentina. Arct. Alp. Res. 22 (3), 215–232. https://doi.org/10.1080/00040851.1990.12002786.

Villalba, R., Boninsegna, J.A., Veblen, T.T., Schmelter, A., Rubulis, S., 1997. Recent trends in tree-rings records from high elevation sites in the Andes of Northern Patagonia. Climatic Change 36, 425–454.

Villalba, R., Lara, A., Boninsegna, J.A., et al., 2003. Large-scale temperature changes across the southern Andes: 20th-century variations in the context of the past 400 years. In: Climatic Change Climate Variability and Change in High Elevation Regions: Past, Present and Future, 25–28 June 2001, vol. 59. Davos, Switzerland, pp. 177–232.

Villa-Martínez, R., Moreno, P.I.(, 2007. Pollen evidence for variations in the southern margin of the westerly winds in SW Patagonia over the last 12,600 years. Quat. Res. 68, 400–409. https://doi.org/10.1016/j.yqres.2007.07.003.

Villa-Martínez, R., Moreno, P.I., Valenzuela, M.A., 2012. Deglacial and postglacial vegetation changes on the eastern slopes of the Patagonian Andes (47°S). Quat. Sci. Rev. 32, 86–99.

Waldmann, N., Anselmetti, F.S., Ariztegui, D., Austin, J.A., Pirouz, M., Moy, C.M., Dunbar, R., 2011. Holocene mass-wasting events in Lago Fagnano, Tierra del Fuego (54°S): implications for paleoseismicity of the Magallanes-Fagnano transform fault. Basin Res. 23 (2), 171–190. https://doi.org/10.1111/j.1365-2117.2010.00489.

Wei, T., Simko, V., 2017. R Package "corrplot": Visualization of a Correlation Matrix. Version 0.84. Available from: https://github.com/taiyun/corrplot.

Żarczyński, M., Tylmann, W., Goslar, T., 2018. Multiple varve chronologies for the last2000 years from the sediments of Lake Żabińskie (northeastern Poland) – comparison of strategies for varve counting and uncertainty estimations. Quat. Geochronol. 47, 107–119. https://doi.org/10.1016/j.quageo.2018.06.001.

Zolitschka, B., 1996. High resolution lacustrine sediments and their potential for palaeoclimatic reconstruction. In: Jones, Bradley, Jouzel (Eds.), Climatic Variations and Forcing Mechanisms of the Last 2000 Years, vol. 141. NATO ASI series, pp. 453–478.

Zolitschka, B., Fey, M., Janssen, S., Maidana, N., Mayr, C., Wulf, S., Haberzettl, T., Corbella, H., Lücke, A., Ohlendorf, C., Schäbitz, F., 2019. Southern Hemispheric westerlies control sedimentary processes of laguna azul (south-eastern Patagonia, Argentina). Holocene 29 (3), 403–420.